IEEE Access
Multidisciplinary | Rapid Review | Open Access Journal

Received August 25, 2017, accepted September 18, 2017, date of publication October 3, 2017, date of current version November 7, 2017.

Digital Object Identifier 10.1109/ACCESS.2017.2758903

Fault-Tolerant Certifiable Control for a V-Tail Remotely Piloted Aircraft System

LUIS GARCÍA-HERNÁNDEZ, CRISTINA CUERNO-REJADO, AND MANUEL PÉREZ-CORTÉS

Department of Aircraft and Spacecraft, Escuela Técnica Superior de Ingeniería Aeronáutica y del Espacio, Technical University of Madrid, 28040 Madrid, Spain

Corresponding author: Luis García-Hernández (luis.garcia.hernandez@alumnos.upm.es)

This work was supported by Grupo Mecánica del Vuelo.

ABSTRACT This paper presents a new approach from a certification standpoint toward the fault-tolerant control (FTC) strategies used to accommodate failures of a Remotely Piloted Aircraft System (RPAS) in non-conventional aerodynamic configuration. The reference aircraft of this paper is the ATLANTE RPA, which has a V-tail. A novel review of the most common accidents and incidents in general and commercial aviation, and in the RPAS sector, has been conducted in order to check the relevance of the proposed failures and the flight phase where they most frequently happen. Damage scenarios are, on the one hand, one locked-in-place flaperon and, on the other hand, propulsion system failure resulting in a gliding flight condition. This second scenario is an original contribution of this paper. The proposed FTC is based on the multiple model switching and tuning technique, and then a classical control is applied to each model in order to ensure the certification criteria. In the case of the propulsion system failure model, a new architecture with airspeed-on-elevator control law is proposed. This controller has been tested using a novel guidance law during the gliding, final approach, and landing phases making use of a flight simulator developed for the ATLANTE RPA. The results obtained highlight the concordance between the regulation requirements and the results for both proposed failures, making it possible for the aircraft to meet the certification requirements, while maintaining a safe condition after failures.

INDEX TERMS Certification, fault-tolerant control (FTC), multiple model switching and tuning (MMST), remotely piloted aircraft system (RPAS), V-tail.

I. INTRODUCTION

The safe operation of Remotely Piloted Aircraft Systems (RPAS) is one of the most important issues affecting their integration in non-segregated airspace. There is still a lot of work to do in many areas in order to achieve this goal. Authorities all around the world are developing new regulations that affect RPAS, their systems, and their operation. Also, many studies are being conducted in the development of new technologies that can be used in RPAS. This progress will allow the required safety level of the operation of RPAS.

One of the main differences between manned aviation and RPAS is the onboard pilot. In the case of a failure happening during flight, the pilot makes use of his/her situational awareness and then makes the necessary decisions for controlling the aircraft. However, as RPAS do not have an onboard pilot, in such conditions the situational awareness of the remote pilot is not as good as it should be and the reconfiguration of the flight control system becomes critical. Thus, many studies are being conducted in fields such as Fault-Tolerant Control (FTC), Fault Detection and Identification (FDI) systems, guidance systems reconfiguration, or Sense and Avoid (S&A) systems.

Sensor, actuator and structural damage are the most common types of studied failures. The sensor faults result in an incorrect measure of the variable of interest for the flight control system. Nevertheless, the actuator failures or structural damage imply the change of the aircraft dynamics, and it is possible the RPA could be uncontrollable if appropriate measures are not taken. The structural damage is usually based on the assumption that a part of the aircraft is lost. Sensor failures are considered in [1]–[3]. References [1]–[11] include actuator faults. Inside the actuator faults category, the elevator and stabiliser faults are studied in [2]–[4] and [6]–[10], whereas rudder malfunctions are presented in [4], [6], [7], [9], and [11], flap failures are included in [6] and [8], and failures related to ailerons are shown in [1] and [11]. Additionally, powerplant problems are addressed in [9]. Structural damage studies are conducted in [1], [9], and [12]–[16]. In the

same way as in the case of actuator faults, the structural damage can be divided into different groups. Wing damage is included in [12]–[14], and vertical tail damage is addressed in [1], [9], [15], and [16].

From the FTC strategies standpoint, there are several possible techniques. On the one hand, passive techniques are usually based on robust controllers and they allow the accommodation of failures that do not result in a large change of the aircraft dynamics. The main advantage of passive methods is the low computational requirements. However, as they do not reconfigure the flight control system after the failure, only a few kinds of faults can be addressed. Also, in the case of increasing the uncertainties of the robustness in the design in order to tolerate more kind of faults, the flying qualities are significantly degraded in fault-free operation. On the other hand, active techniques are based on controller redesign, or the selecting/mixing of predesigned controllers. They can reconfigure the whole flight control system, from the architecture of the controller or the values of the PIDs, to the type of the control, changing the way of controlling the aircraft. The computational cost of these methods is higher than the passive ones. Furthermore, these techniques usually need a FDI system to detect and identify which fault has happened [17]. Passive technique is used in [15]. Active methods can be divided in several techniques. Adaptive control is studied in [3], [7], and [8]. The Model Predictive Control (MPC) technique is used in combination with subspace identification, resulting in Subspace Predictive Control (SPC) in [4], and is also used with MMST, through a technique called Multiple Model Predictive Control (MMPC), in [6]. Control Allocation (CA) is another useful technique that can be found in [10] and [11]. The Interacting Multiple Models (IMM) method is used in [5]. References [1], [2], [9] address the online physical model identification and then use another control strategy such as Inverse Dynamics (ID) or Linear Quadratic Regulation (LQR). The MMST can be used with adaptive control to configure a Model Reference Adaptive Control (MRAC), and also it is possible to combine this last technique with others like LQR. MMST and MRAC techniques are used in [12]–[14] and [16].

Finally, it is important to consider the category of the selected aircraft because it directly relates to the weight or computational capabilities of the aircraft and the redundancy of some critical systems from the flight control system point of view, such as actuators or sensors, for example. In addition, the dynamics of the aircraft and its performances change not only with the category of the RPA, but also with the aerodynamic configuration. The Eagle-Eye rotary wing Unmanned Aerial Vehicle (UAV) is used in [5]. The rest of the references of this manuscript related to FTC use fixed wing aircraft. The aircraft with the lowest weight is the ZAGI UAV in [3]. For the military aircraft category, fighter aircraft like F/A-18, F-16 or Tailless Advanced Fighter Aircraft (TAFA) are the reference aeroplanes in [2], [6]–[8], [12], and [13]. In the general aviation and commuter category, a Cessna 182 is taken for the simulations in [10], whereas a Dornier Do228-202 turboprop aeroplane is included in [1]. Finally, [14] used the NASA Generic Transport Model (GTM) and [4], [9], [11], [15], [16] conducted their studies with the Boeing 747 aeroplane. These last two aircraft models belong to the commercial transport aviation category.

Although many studies of FTC problems have been conducted with satisfactory results and their viability has been demonstrated, there are still issues with the certification requirements. The remotely piloted aerial vehicles with a Maximum Take-Off Weight (MTOW) of more than a specified weight, which depends on each country regulations, must be certified in order for their operation to be allowed. This means that the aircraft and its systems must be in accordance with the corresponding regulation. The certification process affects all aspects of the new aircraft, from its conceptual design to its service life. Nowadays the Authorities of many countries are working on the development of new regulations for RPAS. In the United States there are three categories for the operation of RPAS: public operations, civil operations, and model aircraft operation. In 2016, a new regulation [18] about RPAS with a MTOW of less than 25 kg has been approved by Federal Aviation Administration (FAA). This regulation differences the use of RPAS for working activities and for fun activities. In the European Union, European Aviation Safety Agency (EASA) has published a Notice of Proposed Amendment (NPA) [19] on May 2017 which amends the Advanced Notice of Proposed Amendment (A-NPA) [20] they published on 2015 about the regulatory framework for the operation of drones. In these documents, EASA shows a change in the way the regulation is addressed because the categorization is made depending on the operational risk. In both regulations, RPAS are divided into three different categories: open (low risk operation), specific (medium risk operation), and certified (higher risk operation). The open category is for RPAS whose MTOW is under 25 kg and their operation must satisfy certain requisites. The specific category is for RPAS with a MTOW greater than 25 kg and an operational risk lower than that for the certified category, although some operations using RPAS with a MTOW of less than 25 kg could belong to this category. The certified category is for all RPAS with higher operational risk. On the one hand, the open category is addressed in the NPA, where it is also divided into different groups depending on the MTOW, among other characteristics. On the other hand, the certified category has a regulatory framework similar to manned aviation. The specific category has not been addressed in detail yet. In spite of these EASA proposal of regulation framework, there are still no final regulations approved and it is necessary to specify many particular requirements, as those referred to the hardware and software of the on board systems of RPAS, for example. Thus, in this work some manned aircraft regulations are used. In particular, the regulation SAE-AS94900 [21] refers to the whole aircraft plus the flight control system. Among other aspects, it defines requirements about the Handling Qualities (HQ) of the aircraft in every

TABLE 1. Short-period damping ratio limits (extracted from [23]).

Level	Category A and C flight phases		Category B flight phases	
	Minimum	Maximum	Minimum	Maximum
1	0.35	1.30	0.30	2.00
2	0.25	2.00	0.20	2.00
3	0.15*	-	0.15*	-

* May be reduced at altitudes above 20,000 feet if approved by the procuring activity

TABLE 2. Spiral stability – minimum time to double amplitude (extracted from [23]).

Flight phase category	Level 1	Level 2	Level 3
A & C	12 s	8 s	4 s
B	20 s	8 s	4 s

TABLE 3. Maximum roll-mode time constant (extracted from [23]).

Flight phase category	Level		
	1	2	3
A	1.0 s	1.4 s	10 s
B	1.4 s	3.0 s	10 s
C	1.0 s	1.4 s	10 s

TABLE 4. Minimum Dutch roll frequency and damping (extracted from [23]).

Flight phase		Min. ξ_d	Min $\xi_d\omega_{n_d}$ rad/s	Min ω_{n_d} rad/s
Level	Category			
1	A	0.19	0.35	1.0
	B	0.08	0.15	0.4
	C	0.08	0.15	1.0
2	All	0.02	0.05	0.4
3	All	0	-	0.4

considered scenario. MIL-DTL-9490E [22] is the previous version of the SAE-AS94900 regulation. In this document, depending on the flight scenario, the MIL-F-8587 regulation [23] is cited to establish requirements about many aspects of the aircraft, such as the damping and the frequency of the eigenvalues of the aircraft, considering it as a rigid body. As the atmosphere could include turbulence, the turbulence model must be considered to obtain realistic results. In fact, turbulence must be considered not only in the autopilot and the flight mechanics, but also in the design stage for structural parts, for example. The previous regulations establish the way in which the turbulence should be taken into account. Therefore, the flight control systems must be designed in a way that all the certification requirements shall be met. This means that many control techniques, such as adaptive ones, for example, are not valid from the certification standpoint. As an example, in Table 1, Table 2, Table 3, Table 4, and Table 5, the MIL-F-8785 requirements for the short period, spiral, roll, and Dutch roll modes, and roll performance, respectively, of the Class I aircraft are shown. The Class I aircraft are those with a MTOW of less than 5000 kg.

TABLE 5. Roll performance: time to achieve the following bank angle change (extracted from [23]).

Level	Category A (60º)	Category B (60º)	Category C (30º)
1	1.3 s	1.7 s	1.3 s
2	1.7 s	2.5 s	1.8 s
3	2.6 s	3.4 s	2.6 s

Next, a study about the manned aviation accidents and incidents is detailed. According to the Boeing statistical summary for commercial jet aeroplane accidents [24], the final approach and landing phases (47%), and cruise phase (12%) are the most common flight phases in which the accidents happen. The onboard fatalities are respectively, in percentage, 47% and 24%. The main causes of the accidents, ordered from the most to the least probable, are loss of control – in flight (LOC-I), runway excursion (RE), and controlled flight into or toward terrain (CFIT). Similar studies have been conducted by Comisión de Investigación de Accidentes e Incidentes de Aviación Civil (CIAIAC) in Spain, by Air Safety Institute (ASI), and by EASA at Europe level, among others. The annual review of 2015 elaborated on by CIAIAC [25] showed that the number of aircraft accidents with a MTOW up to 2250 kg (86%) are much higher than those aircraft with a MTOW of more than 2250 kg (14%). The main causes of the accidents and incidents are, in this case, Airprox/ACAS alert/loss of separation/(near) midair collisions (MAC), CFIT, collision with an obstacle during Take-Off and Landing (CTOL), and fuel related. Regarding the flight phase, final approach (33%), landing (16%) and cruise (16%) phases are the most common. ASI provides the percentage of the accident causes in its review entitled "Accident during flight instruction: a review" [26], differentiating if the percentage is for primary dual, primary solo, or advanced dual instruction. The take-off, landing and go-around (50% for primary dual, 80% for primary solo) and mechanical / power loss (20% primary dual, 5% primary solo) are the most common causes. On the one hand, during take-off, landing and go-around phases for primary dual, the loss of control (49%) and stalls or hard landing (32%) are the most frequent causes. The same results are obtained for primary solo, with a percentages about 50% and 41% for the loss of control and stalls or hard landings causes, respectively. On the other hand, the mechanical and power loss accidents study showed that a powerplant failure (including unexplained power loss, powerplant and fuel system) is the most common, with a percentages of 79% for primary dual and 64% for primary solo. The airframe, flight controls or electrical failure are the third most frequent causes for both types of instruction, with a probability of 12% and 13%, respectively. The electrical failures have been included in the flight control and airframe category due to the relevance of this system to the actuation system in the general aviation category aeroplanes, where the tendency is to design More

Electrical Vehicles (MEV) with electro-mechanical or electrical actuators. Finally, EASA [27] showed that the most frequent flight phases for the accidents which happened in 2015 for the general aviation category were landing (45%), take-off (17%), cruise flight (13%) and final approach (12%) phases. During 2016, the priority key risks areas of non-commercial operations identified by EASA in its 2017 annual review [28] were the aircraft upset (47%) and terrain collisions (23%). Additionally, in the same review, a section about the incidents and accidents involving both RPAS/UAS and civil aircraft is included. The first priority key risk area for the RPAS/UAS category is the aircraft upset (50%), where the main cause is the loss of control. As it has been explained, these reviews show similar results: the final approach, landing and cruise flight are the most critical, and one of the main causes is usually the powerplant failure. This type of failure is especially critical in single-engine aeroplanes, due to the emergency landing manoeuvre.

In the military field, RPAS have had a longer operational life, so it is possible to study the statistics for accidents and incidents involving military RPAS. In the MS thesis entitled "Accidents investigation of unmanned aircraft – RPAS" [29], several studies about RPAS accidents reports were conducted. Aircraft Accident Investigation Board (AIB) studied 19 accidents of the MQ-1B, also known as Predator, between 2011 and 2013. Mechanical failures were the most common cause, which is present in 11 accidents (58%). During the Iraq war, there were more than 100 reported accidents of RPAS, being the Raven RPA (64%) and the Shadow RPA (12.8%) the aerial vehicles with more investigated accidents. In the case of the Raven RPA (RQ-11B), the data link loss is the most frequent cause (44%), followed by electronic (7%) and mechanical (5%) causes. Mechanical (63%) problems are the most probable failure type present in the operation of the Shadow (RQ-7) RPA. Finally, this document presents a study into the accidents found on different web sites. The results highlighted that the mechanical failure (35.8%) is the most frequent kind of failure. The report from Federal Aviation Administration (FAA) of 2004 [30] analyses the accidents of the Hunter, Shadow, Pioneer, Predator, and Global Hawk RPAS, whose results are included in Fig. 1. The most frequent flight phases for the accidents of the Pioneer, Hunter and Predator RPAS are the landing (68%, 47%, and 87% respectively) and take-off (10%, 20%, 13%, respectively), according to [31].

In this work, the reference aircraft is the ATLANTE RPA, which has a non-conventional aerodynamic configuration with a V-tail. The reason the ATLANTE has been chosen as the reference aircraft is that the company Grupo Mecánica del Vuelo (GMV) has relevant data of this aircraft, and GMV partly supports this work. It is important to note that the ATLANTE is a military fixed-wing single-engine aircraft, with no redundant controls. This characteristic makes the actuator and engine failures or structural damage more critical. Two failure scenarios have been studied in this paper: one is a locked-in-place flaperon, and the other one is engine

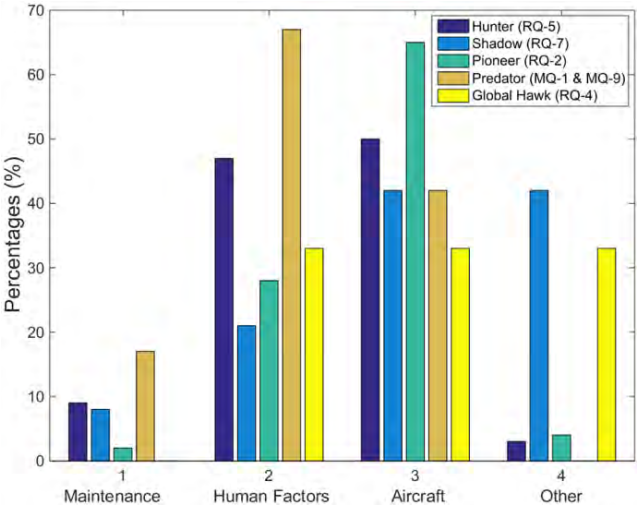

FIGURE 1. Statistic of RPAS accidents of the document [30].

failure, with total power loss and stopped propeller with the possibility of changing its pitch to feather it. The strategy used for the FTC problem is MMST because it allows changes between different models to be taken into account during the design stage, while keeping a low computational cost and an accuracy in direct relation to the precision of the used models. Furthermore, each model of the multiple models can be designed according to the regulation standards, which gives this method the possibility of passing the certification process, and tuning it to accommodate the typical nonlinearities present inside the flight envelope of all aeroplanes. Therefore, MMST technique with classical control theory for a nonlinear system with actuator and powerplant failures has been applied to a RPAS with a V-tail non-conventional aerodynamic configuration. The results of the proposed method have been obtained with a flight simulator built for the ATLANTE RPA, simulating the loiter and landing phases according to the conclusions about the previous accident and incident review. As it can be observed, the reference RPA belongs to the general aviation category of the manned aeroplanes. So, the techniques developed here could be easily applied to that category to reduce the number of accidents and incidents. The main contributions of this manuscript are: (1) the certification standpoint for the FTC problem in the RPAS field; (2) the use of a V-tail reference aircraft, which belongs to a widely used non-conventional aerodynamic configuration that has not been addressed in detail in previous research studies; and (3) a novel engine failure scenario considered from the FTC and guidance system reconfiguration point of view.

This paper is organized as follows: In Section II, the reference aircraft is explained in detail, and the considered failure scenarios with the trimmed flight condition are commented on. Section III includes the aircraft dynamic model after the failure, and the autopilot design process, highlighting the regulation focus of the results. The simulator is used to validate the results in Section IV. Finally, Section V contains concluding remarks.

TABLE 6. ATLANTE RPA main parameters [32], [33]

Parameter	Units	Value
Length	m	5.47
Wingspan	m	8.00
Height	m	1.99
Reference wing area	m^2	6.71
Mean Aerodynamic Chord (MAC)	m	0.87
Tail arm	m	3.03
V-tail reference area	m^2	1.48
V-tail dihedral	º	37
MTOW	kg	570
Maximum speed (True Airspeed, TAS)	m/s	60
Cruising speed (True Airspeed, TAS)	m/s	37.5
Maximum altitude	m	6000
Cruise altitude	m	3000
Endurance	h	Over 10 h

m = meter, º = degree, s = second, kg = kilogram, h = hour.

II. REFERENCE AIRCRAFT AND FAILURE SCENARIOS

A. REFERENCE AIRCRAFT DATA

As it was said in the introduction, the reference aircraft is the ATLANTE RPA. It has a V-tail, which is a typical non-conventional aerodynamic configuration present in many RPAS. The use of a RPAS with a V-tail is one of the original contributions of this paper. Opposite to the conventional tails, V-tails could result in a coupling between the longitudinal and lateral-directional problems. The control surfaces available for this aircraft are two flaperons (one in each wing semispan) and four ruddervators (two in each V-tail panel). The flaperons are control surfaces that can be differentially deflected, which allows them the simultaneous behave as flaps and ailerons. The ruddervators are the control surfaces of the V-tail. In the same way as in the case of flaperons, a pair of symmetric ruddervators can be differentially deflected symmetrically or anti-symmetrically, behaving as an elevator or a rudder, respectively. The main data [32], [33] about the ATLANTE are included in Table 6.

B. AIRCRAFT DYNAMIC MODEL CHARACTERISTICS ESTIMATION

The first step to characterize the ATLANTE is to obtain the mass model, making use of [34], [35]. This model provides the weight of each part of the aircraft and the Centre of Gravity (CG) position. Next, it is possible to estimate the aerodynamic model with a combination of Digital DATCOM code [36], Torenbeek [34], Roskam [37], [38], and Raymer [39] methods, and NACA Report No. 823 about V-tails [40]. Therefore, the aerodynamic model is based on the aerodynamic stability derivatives method. The drag polar obtained through different methods is shown in Fig. 2. Torenbeek method has been selected as the true drag polar. Fig. 3 includes the aerodynamic efficiency.

Once the mass and the aerodynamic methods are computed, it is possible to estimate the performances of the aircraft with the propulsive model. A study about the change of the power provided by the engine with the altitude and

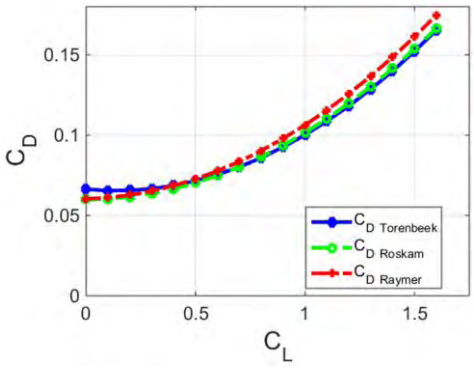

FIGURE 2. Drag polar of the ATLANTE RPA using [34], [38], [39].

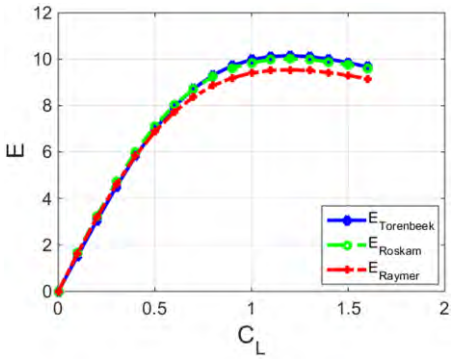

FIGURE 3. Aerodynamic efficiency of the ATLANTE RPA using [34], [38], [39].

the throttle position has been conducted. Furthermore, it is necessary to obtain the propeller efficiency, which depends on the speed of the aircraft, the power provided by the engine, and the propeller revolutions.

Reference [41] has been used to estimate the propeller efficiency model. The performances obtained making use of the mass, aerodynamic, and propulsive models for the maximum propeller efficiency are shown in Fig. 4, where "OEW" is the Operational Empty Weight, "Pnec" is the necessary power for cruising flight, and "Pavailable" is the available power provided by the propeller. The maximum speed is around 58 m/s, giving a relative error of 3.3%, and the theoretical ceiling is 6000 m. As it can be seen, the speed and the ceiling values are in accordance with the data provided by the manufacturer of the aircraft, therefore the models are validated.

The procedure explained before is analogous to that conducted in [42], taking into account the distinctive features of the ATLANTE. Finally, the landing gear model is based on [43].

C. FAILURE SCENARIOS AND TRIM CONDITIONS

The relevance of each kind of failure could change depending on the design mission of the aircraft. Additionally, the design mission results in a final aircraft category and performance characteristics. As it was said in the introduction, the category

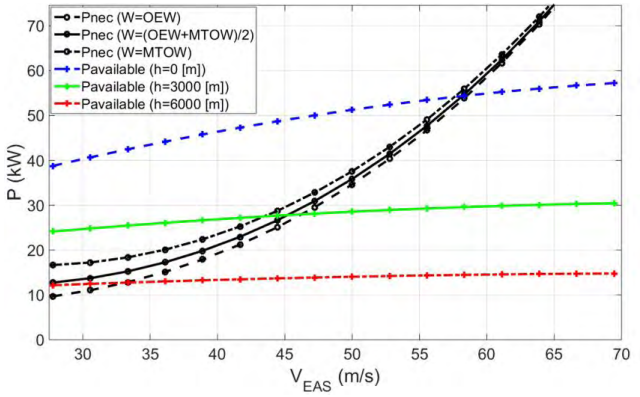

FIGURE 4. Performances of the ATLANTE RPA for maximum propeller efficiency and maximum engine power.

of the aircraft directly relates to the redundancy of different systems or the computational capabilities from the FTC point of view. For example, in the case of two-engine aircraft, the loss of one engine is less critical from the guidance system reconfiguration standpoint than in the case of a single-engine aircraft. In the same way, if the aircraft has redundant controls or sensors, the failure of one control surface or sensor results in a less hazardous scenario. Structural elements loss could be more relevant in military aircraft, especially in those who are going to be operated under enemy fire. In any case, the actuators and structural elements failures are the most critical faults from the control point of view due to the change of the aircraft dynamics. Additionally, the number of possible considered failures is also related to the computational capabilities. The higher the computational capabilities are, the greater the number of failures which can be taken into account. Therefore, the designers must select which kind of failures need to be addressed in order to guarantee the safe operation of the aircraft in presence of the most critical and/or common expected failures.

One considered failure scenario is the lock-in-place of the left flaperon at 5°. The other failure is the total loss of power provided by the powerplant, although the control of the propeller pitch is still available. So, for the second case, the propeller is feathered in order to reduce the drag that it provides according to the model included in [44]. These two kind of failures have been selected according to the accidents and incidents study included in the introduction. On the one hand, the flaperon lock-in-place fault is an example of mechanical failure which allows to evaluate the flap and aileron lock-in-place faults at the same time. On the other hand, one of the worst failure scenarios for a single-engine aircraft is the total power loss, so, the powerplant failure is also addressed. In addition, the powerplant failure resulting in a total power loss is an original contribution of this manuscript. Next, the trim conditions are explained.

First, it is necessary to trim the lateral-directional problem. In the locked-in-place flaperon case, this is accomplished by deflecting the symmetric flaperon to the same position than the faulty one. In the engine failure case, as the ATLANTE is a single-engine aeroplane, the lateral-directional problem is trimmed itself by maintaining the symmetry of the aircraft. Once the lateral-directional problem is trimmed, it is needed to trim the longitudinal one. The next expressions allow the obtainment of the deflection of the elevator and the Angle of Attack (AoA):

$$mg/\left(0.5\rho V^2 S_{ref}\right) = C_{L_{cruise}} \tag{1}$$

$$C_{L_{cruise}}\cos\theta = C_{L_0} + C_{L_\alpha}\alpha + C_{L_{\delta_e}}\delta_e + C_{L_{\delta_{r_{trim}}}}\delta_{r_{trim}} + C_{L_{\delta_f}}\delta_f + C_{L_{\delta^*}}\delta^* \tag{2}$$

$$C_{m_0} + C_{m_\alpha}\alpha + C_{m_{\delta_e}}\delta_e + C_{m_{\delta_{r_{trim}}}}\delta_{r_{trim}} + C_{m_{\delta_f}}\delta_f + C_{m_{\delta^*}}\delta^* = 0 \tag{3}$$

In the previous expressions, S_{ref} is the planform wing surface area, ρ is the atmospheric density of the air in the reference flight condition, V is the aircraft airspeed in TAS, m is the mass of the aircraft, g is the gravity acceleration, α is the AoA of the aircraft, θ is the aircraft pitch angle, δ^* is the faulty control surface position, δ_f is the fault-free flaperon deflection, δ_e is the elevator deflection, and $\delta_{r_{trim}}$ is the trim deflection of the rudder as an elevator, and the remaining coefficients as C_{L_α}, C_{L_0}, $C_{L_{\delta_e}}$, C_{m_0}, C_{m_α}, etc. are the aerodynamic coefficients of the aircraft. In the case of no flaperon failure, the previous (1-3) expressions are valid by substituting $\delta^* = 0$ and $\delta_f = 0$. This means that the flaperons are not used to trim the aircraft, and only the elevator, and the rudder as an elevator, if applicable, are used for it.

It is important to remark the need for the aerodynamic study in order to guarantee that the aircraft can be trimmed leaving all the possible controls available for their use.

First, for the trim study during the cruise phase, where flaps are not deflected and only aileron deflections are commanded, it is important to note that the locked flaperon provides not only rolling and yawing moments as an aileron, but also drag and lift forces and pitching moment, as a flap, because the fault-free flaperon could be in a position that is not the anti-symmetric one. Then, as it was explained before, the fault-free flaperon must be deflected at the same position (symmetrically) as the faulty flaperon in order to maintain the symmetry of the aircraft. This means that the flaperons are behaving as simple flaps. Once the lateral-directional problem is trimmed it is necessary to compensate the increase in the pitching moment and in the lift force with the elevator. Also, the variation in the drag force results in a variation of the speed, which must be compensated with the throttle position. It is possible that the required elevator deflection to trim the longitudinal problem could be near to the maximum allowable position, and the available range for deflecting the elevator from that moment would be null in one direction. Furthermore, the effectiveness of the control surfaces significantly decreases with the deflection for positions that are greater than 12° or 15°, depending on the control surface design, aggravating the new flight condition. To avoid

TABLE 7. Control deflections to trim the aircraft.

Condition	δ_e (º)	δ_r (º)
Fault-free	-0.3	0
-25º locked-in-place flaperon	6.5	6.5
-20º locked-in-place flaperon	6.9	6.9
-15º locked-in-place flaperon	6.5	6.5
-10º locked-in-place flaperon	9.8	0
-5º locked-in-place flaperon	4.7	0
5º locked-in-place flaperon	-5.4	0
10º locked-in-place flaperon	-10.5	0
15º locked-in-place flaperon	-6.8	-6.8
20º locked-in-place flaperon	-7.2	-7.2
25º locked-in-place flaperon	-6.7	-6.7

this situation, the rudder could be trimmed as an elevator at one intermediate position to help to the elevator for trimming the aircraft, resulting in a lower elevator deflection. This new condition gives a valid range for the deflection of both the elevator and the rudder. In order to take this into account, in this study if the lock-in-place flaperon fault happens at a position of more than 10°, then the rudder is trimmed as elevator, and from this position is behaving as a rudder (anti-symmetric deflection). In Table 7 some different trimmed conditions are presented to show the results of this study. The non-symmetric behaviour of the deflections is due to the lift of the V-tail in cruise flight, and the lower value for 25° locked-in-place faults than for 20° is due to the nonlinearity of the control surfaces. The flight condition is defined by cruise flight at 48.6 m/s, and 3000 m of altitude.

Secondly, for the autopilot design, as only there is one fault-free flaperon, the deflection as flaps is not possible except for the position of the locked-in-place flaperon. In addition, the deflection demanded by the autopilot for the fault-free flaperon as an aileron provides not only rolling (C_l) and yawing (C_n) moments, but also drag (C_D) and lift (C_L) forces, and pitching (C_m) moment. Therefore, the longitudinal and lateral-directional problems are coupled.

Once the aircraft has been trimmed, it is possible to address the dynamic model definition after the failure in the next section.

III. DYNAMIC MODEL AND AUTOPILOT DESIGN

A. FAULT-TOLERANT CONTROL STRATEGY FOR THE AUTOPILOT

For the FTC problem, it is assumed that an ideal FDI system is supervising the condition of the aircraft and it can instantaneously detect the failures of this work. Fig. 5 shows a diagram of the subspaces that must be studied in order to achieve the required level of robustness, which depends on the overlapping of subspaces in this case. Each subspace corresponds to each failure aircraft model, and inside that subspace, the classical autopilot can be tuned to fit the non-linearity of each variable along the whole flight envelope, as in a classical approach.

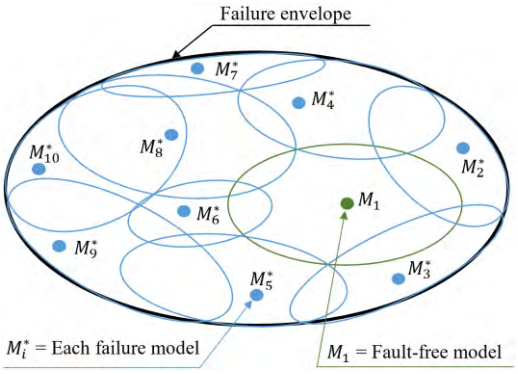

FIGURE 5. Required MMST models to guarantee the robustness of the design.

B. AIRCRAFT DYNAMIC MODEL EXPRESSIONS

In Fig. 6, the aerodynamic and propulsive forces and moments, and the linear speeds and angular rates of an aircraft are presented.

The flight dynamic expressions of an aircraft [45] are:

$$-mg\sin\theta + F_{T_X} + F_{A_X} = m(\dot{u} - rv + qw) \tag{4}$$

$$mg\cos\theta\sin\phi + F_{T_Y} + F_{A_Y} = m(\dot{v} + ru - pw) \tag{5}$$

$$mg\cos\theta\cos\phi + F_{T_Z} + F_{A_Z} = m(\dot{w} - qu + pv) \tag{6}$$

$$L_T + L_A = \left(I_z - I_y\right)qr - I_{xz}pq + I_x\dot{p} - I_{xz}\dot{r} \tag{7}$$

$$M_T + M_A = -\left(I_z - I_x\right)pr + I_{xz}(p^2 - r^2) + I_y\dot{q} \tag{8}$$

$$N_T + N_A = -\left(I_x - I_y\right)pq + I_{xz}qr + I_z\dot{r} - I_{xz}\dot{p} \tag{9}$$

The aerodynamic and propulsive forces and moments must be linearised around some particular flight condition. Taking this reference condition after a flaperon lock-in-place failure, the linearised aerodynamic forces and moments are:

$$F_{A_X} = X_0 + X_u u + X_w w + X_{\delta_e}\delta_e + X_{\delta_f}\delta_f + X_{\delta^*}\delta^* + X_{\delta_{r_{trim}}}\delta_{r_{trim}} \tag{10}$$

$$F_{A_Y} = Y_v v + Y_p p + Y_r r + Y_{\delta_r}\delta_r + Y_{\delta_f}\delta_f + Y_{\delta^*}\delta^* \tag{11}$$

$$F_{A_Z} = Z_0 + Z_u u + Z_w w + Z_{\dot{w}}\dot{w} + Z_q q + Z_{\delta_e}\delta_e + Z_{\delta_f}\delta_f + Z_{\delta_{r_{trim}}}\delta_{r_{trim}} + Z_{\delta^*}\delta^* \tag{12}$$

$$L_A = L_v v + L_p p + L_r r + L_{\delta_r}\delta_r + L_{\delta_f}\delta_f + L_{\delta^*}\delta^* \tag{13}$$

$$M_A = M_0 + M_u u + M_w w + M_{\dot{w}}\dot{w} + M_q q + M_{\delta_e}\delta_e + M_{\delta_{r_{trim}}}\delta_{r_{trim}} + M_{\delta_f}\delta_f + M_{\delta^*}\delta^* \tag{14}$$

$$N_A = N_v v + N_p p + N_r r + N_{\delta_r}\delta_r + N_{\delta_f}\delta_f + N_{\delta^*}\delta^* \tag{15}$$

The new aircraft dynamic model is obtained by combining these expressions with (4-9). Next, small perturbations around the reference flight condition are introduced in the model. The subscript *s* refers to the reference flight condition. The term due to $\delta_{r_{trim}}$ in the longitudinal problem has not been perturbed because the rudder does not provide drag and lift forces nor pitching moment. It is very important to note that

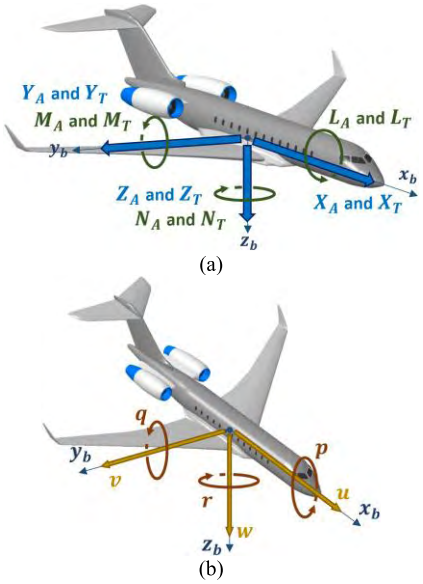

FIGURE 6. (a) Aerodynamic and propulsive forces and moments, and (b) Linear speeds and angular rates.

the faulty control surface cannot change its position after the lock-in-place fault, so its term does not have a perturbed part. Subtracting the reference condition and neglecting second order terms, the final model is as follows:

$$\begin{aligned}
&-mg\cos\theta_s\Delta\theta+\Delta F_{T_X}\\
&\quad+\left(X_u\Delta u+X_w\Delta w+X_{\delta_e}\Delta\delta_e+X_{\delta_f}\Delta\delta_f\right)\\
&=m(\Delta\dot{u}-\Delta rv_s-r_s\Delta v+\Delta qw_s+q_s\Delta w) &(16)\\
&mg\cos\theta_s\cos\phi_s\Delta\phi-mg\sin\theta_s\sin\phi_s\Delta\theta+\Delta F_{T_Y}\\
&\quad+\left(Y_v\Delta v+Y_p\Delta p+Y_r\Delta r+Y_{\delta_r}\Delta\delta_r+Y_{\delta_f}\Delta\delta_f\right)\\
&=m(\Delta\dot{v}+\Delta ru_s+r_s\Delta u-\Delta pw_s-p_s\Delta w) &(17)\\
&-mg\sin\theta_s\cos\phi_s\Delta\theta-mg\cos\theta_s\sin\phi_s\Delta\phi+\Delta F_{T_Z}\\
&\quad+\left(Z_u\Delta u+Z_w\Delta w+Z_{\dot{w}}\Delta\dot{w}+Z_q\Delta q+Z_{\delta_e}\Delta\delta_e+Z_{\delta_f}\Delta\delta_f\right)\\
&=m\left(\Delta\dot{w}-\Delta qu_s-q_s\Delta u+\Delta pv_s+p_s\Delta v\right) &(18)\\
&\Delta L_T+\left(L_v\Delta v+L_p\Delta p+L_r\Delta r+L_{\delta_r}\Delta\delta_r+L_{\delta_f}\Delta\delta_f\right)\\
&=\left(I_z-I_y\right)(\Delta qr_s+q_s\Delta r)-I_{xz}(\Delta pq_s+p_s\Delta q)\\
&\quad+I_x\Delta\dot{p}-I_{xz}\Delta\dot{r} &(19)\\
&\Delta M_T+(M_u\Delta u+M_w\Delta w+M_{\dot{w}}\Delta\dot{w}\\
&\qquad+M_q\Delta q+M_{\delta_e}\Delta\delta_e+M_{\delta_f}\Delta\delta_f)\\
&=-(I_z-I_x)(\Delta pr_s+p_s\Delta r)+I_{xz}(2p_s\Delta p-2r_s\Delta r)+I_y\Delta\dot{q} &(20)\\
&\Delta N_T+\left(N_V\Delta v+N_p\Delta p+N_r\Delta r+N_{\delta_r}\Delta\delta_r+N_{\delta_f}\Delta\delta_f\right)\\
&=-\left(I_x-I_y\right)(\Delta pq_s+p_s\Delta q)\\
&\quad+I_{xz}(\Delta qr_s+q_s\Delta r)+I_z\Delta\dot{r}-I_{xz}\Delta\dot{p} &(21)
\end{aligned}$$

The next step is to define the reference flight condition. This condition is usually defined as a symmetric ($v_s=\beta_s=0$) rectilinear ($p_s=q_s=r_s=\dot{\phi}_s=\dot{\theta}_s=\dot{\psi}_s=0$) flight, with leveled wings ($\phi_s=0$) in stability axes ($w_s=\alpha_s=0$). Additionally, $w=u_s\alpha$ and $v=u_s\beta$. In accordance with these previous assumptions, the final equations of the flight dynamics model are:

$$\begin{aligned}
&-mg\cos\theta_s\Delta\theta+\Delta F_{T_X}\\
&\quad+\left(X_u\Delta u+X_\alpha\Delta\alpha+X_{\delta_e}\Delta\delta_e+X_{\delta_f}\Delta\delta_f\right)\\
&=m\Delta\dot{u} &(22)\\
&mg\cos\theta_s\Delta\phi+\Delta F_{T_Y}\\
&\quad+\left(Y_\beta\Delta\beta+Y_p\Delta p+Y_r\Delta r+Y_{\delta_r}\Delta\delta_r+Y_{\delta_f}\Delta\delta_f\right)\\
&=m\left(u_s\Delta\dot{\beta}+\Delta ru_s\right) &(23)\\
&\quad-mg\sin\theta_s\Delta\theta+\Delta F_{T_Z}\\
&\quad+\left(Z_u\Delta u+Z_\alpha\Delta\alpha+Z_{\dot{\alpha}}\Delta\dot{\alpha}+Z_q\Delta q+Z_{\delta_e}\Delta\delta_e+Z_{\delta_f}\Delta\delta_f\right)\\
&=m\left(u_s\Delta\dot{\alpha}-\Delta qu_s\right) &(24)\\
&\Delta L_T+\left(L_\beta\Delta\beta+L_p\Delta p+L_r\Delta r+L_{\delta_r}\Delta\delta_r+L_{\delta_f}\Delta\delta_f\right)\\
&=I_x\Delta\dot{p}-I_{xz}\Delta\dot{r} &(25)\\
&\Delta M_T+(M_u\Delta u+M_\alpha\Delta\alpha+M_{\dot{\alpha}}\Delta\dot{\alpha}\\
&\qquad+M_q\Delta q+M_{\delta_e}\Delta\delta_e+M_{\delta_f}\Delta\delta_f)=I_y\Delta\dot{q} &(26)\\
&\Delta N_T+\left(N_\beta\Delta\beta+N_p\Delta p+N_r\Delta r+N_{\delta_r}\Delta\delta_r+N_{\delta_f}\Delta\delta_f\right)\\
&=I_z\Delta\dot{r}-I_{xz}\Delta\dot{p} &(27)
\end{aligned}$$

Finally, the coefficients of the previous expressions are:

$$\begin{aligned}
X_u&=\rho u_sS_{ref}\left(\frac{1}{2}\left(C_{T_{X_{\hat{u}}}}-C_{D_{\hat{u}}}\right)-C_{Z_s}\tan\theta_s\right) &(28)\\
X_\alpha&=\rho u_sS_{ref}/2\left(C_{L_s}-C_{D_\alpha}\right) &(29)\\
X_{\delta_e}&=-\rho u_s^2S_{ref}C_{D_{\delta_e}}/2 &(30)\\
X_{\delta_f}&=-\rho u_s^2S_{ref}C_{D_{\delta_f}}/2 &(31)\\
Y_\beta&=\rho u_s^2S_{ref}C_{Y_\beta}/2 &(32)\\
Y_p&=\rho u_sS_{ref}bC_{Y_{\hat{p}}}/4 &(33)\\
Y_r&=\rho u_sS_{ref}bC_{Y_{\hat{r}}}/4 &(34)\\
Y_{\delta_r}&=\rho u_s^2S_{ref}C_{Y_{\delta_r}}/2 &(35)\\
Y_{\delta_f}&=0 &(36)\\
Z_u&=\rho u_sS_{ref}\left(-\frac{1}{2}C_{L_{\hat{u}}}+C_{Z_s}\right) &(37)\\
Z_\alpha&=\rho u_s^2S_{ref}\left(-C_{L_\alpha}-C_{D_s}\right)/2 &(38)\\
Z_{\dot{\alpha}}&=\rho u_s^2S_{ref}(-C_{L_\alpha}-C_{D_s})/2 &(39)\\
Z_q&=-\rho u_sS_{ref}\bar{c}C_{L_{\hat{q}}}/4 &(40)\\
Z_{\delta_e}&=-\rho u_s^2S_{ref}C_{L_{\delta_e}}/2 &(41)\\
Z_{\delta_f}&=-\rho u_s^2S_{ref}C_{L_{\delta_f}}/2 &(42)\\
L_\beta&=\rho u_s^2S_{ref}bC_{l_\beta}/2 &(43)\\
L_p&=\rho u_sS_{ref}b^2C_{l_{\hat{p}}}/4 &(44)\\
L_r&=\rho u_sS_{ref}b^2C_{l_{\hat{r}}}/4 &(45)\\
L_{\delta_r}&=\rho u_s^2S_{ref}bC_{l_{\delta_r}}/2 &(46)\\
L_{\delta_f}&=\rho u_s^2S_{ref}bC_{l_{\delta_f}}/2 &(47)\\
M_u&=\rho u_sS_{ref}\bar{c}C_{m_{\hat{u}}}/2 &(48)\\
M_\alpha&=\rho u_s^2S_{ref}\bar{c}C_{m_\alpha}/2 &(49)\\
M_{\dot{\alpha}}&=\rho u_sS_{ref}\bar{c}^2C_{m_{\hat{\dot{\alpha}}}}/4 &(50)
\end{aligned}$$

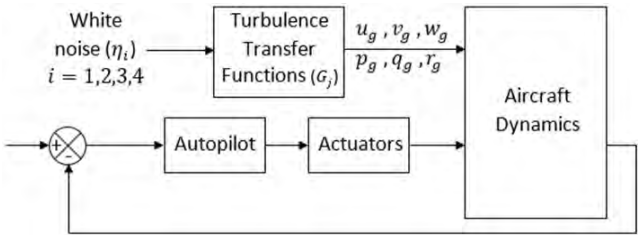

FIGURE 7. Turbulence input to the aircraft dynamics.

$$M_q = \rho u_s S_{ref} \bar{c}^2 C_{m_{\hat{q}}}/4 \quad (51)$$
$$M_{\delta_e} = \rho u_s^2 S_{ref} \bar{c} C_{m_{\delta_e}}/2 \quad (52)$$
$$M_{\delta_f} = \rho u_s^2 S_{ref} \bar{c} C_{m_{\delta_f}}/2 \quad (53)$$
$$N_\beta = \rho u_s^2 S_{ref} b C_{n_\beta}/2 \quad (54)$$
$$N_p = \rho u_s S_{ref} b^2 C_{n_{\hat{p}}}/4 \quad (55)$$
$$N_r = \rho u_s S_{ref} b^2 C_{n_{\hat{r}}}/4 \quad (56)$$
$$N_{\delta_r} = \rho u_s^2 S_{ref} b C_{n_{\delta_r}}/2 \quad (57)$$
$$N_{\delta_f} = \rho u_s^2 S_{ref} b C_{n_{\delta_f}}/2 \quad (58)$$

The term $\bar{c}$ is the MAC, b is the wingspan, $\hat{u} = u/u_s$ is the dimensionless longitudinal speed, $\hat{p} = pb/(2u_s)$, $\hat{q} = q\bar{c}/(2u_s)$, and $\hat{r} = rb/(2u_s)$ are the dimensionless angular rates, $\hat{\dot{\alpha}} = \dot{\alpha}\bar{c}/(2u_s)$ is the dimensionless AoA variation rate, and the rest of the parameters as $C_{D_{\hat{u}}}$, C_{Z_s}, C_{L_s}, C_{D_α}, $C_{D_{\delta_e}}$, $C_{D_{\delta_f}}$, $C_{L_{\hat{u}}}$, C_{L_α}, etc. are the dimensionless aerodynamic coefficients that describe the behaviour of the aircraft in relation to the different variables. These last coefficients can be estimated using [34], [36]–[38], [40]. With (22-27) it is possible to build the state-space model through the A and B typical matrices.

C. TURBULENCE MODEL EXPRESSIONS

Next, the introduction of the turbulence terms is explained. There are different models for taking into account the turbulence. In this work, the Dryden approximation is taken because it is possible to express it analytically. The Dryden model consists of a white noise which is coloured through the transfer functions of the turbulence models as in Fig. 7. It is important to note that the term q_g is derived from the w_g term, and the r_g term comes from the v_g contribution, so only four parameters of white noise must be introduced, one for each linear speed and another one for roll rate contribution [46]. Those transfer functions [47] are:

$$\frac{u_g}{\eta_1} = G_u = \sigma_u \frac{\sqrt{2V/(L_u\pi)}}{s + V/L_u} \quad (59)$$

$$\frac{v_g}{\eta_2} = G_v = \sigma_v \sqrt{3V/(2\pi L_v)} \frac{s + V/\left(2\sqrt{3}L_v\right)}{(s + V/(2L_v))^2} \quad (60)$$

$$\frac{w_g}{\eta_3} = G_w = \sigma_w \sqrt{3V/(2\pi L_w)} \frac{s + V/\left(2\sqrt{3}L_w\right)}{(s + V/(2L_w))^2} \quad (61)$$

$$\frac{p_g}{\eta_4} = G_p = \sigma_w \sqrt{0.8V} \left(\frac{\pi}{4b}\right)^{\frac{7}{6}} / (2L_w)^{\frac{1}{3}} \frac{1}{s + \pi V/(4b)} \quad (62)$$

$$\frac{q_g}{\eta_3} = G_q = \sigma_w \frac{\pi}{4b} \sqrt{\frac{3V}{2\pi L_w}} \frac{s\left(s + V/\left(2\sqrt{3}L_w\right)\right)}{(s + \pi V/(4b))\,(s + V/(2L_w))^2} \quad (63)$$

$$\frac{r_g}{\eta_2} = G_r = \sigma_v \frac{\pi}{3b} \sqrt{\frac{3V}{2\pi L_v}} \frac{s\left(s + V/\left(2\sqrt{3}L_v\right)\right)}{(s + \pi V/(3b))\,(s + V/(2L_v))^2} \quad (64)$$

Where σ_u, σ_v, and σ_w represent the turbulence intensities and L_u, L_v, and L_w are the turbulence scale lengths. The value of these last three parameters depends on the regulations [23], [47], but both references result in the same transfer function after substituting the turbulence scale lengths. For this work, the values for the six coefficients can be found in [47].

The previous turbulence equations can be taken into account in the aircraft dynamic model, resulting in the following expressions:

$$-mg\cos\theta_s\Delta\theta + \Delta F_{T_X} + \left(X_u\left(\Delta u + u_g\right) + X_\alpha\left(\Delta\alpha + \alpha_g\right) + X_{\delta_e}\Delta\delta_e + X_{\delta_f}\Delta\delta_f\right) = m\Delta\dot{u} \quad (65)$$

$$mg\cos\theta_s\Delta\phi + \Delta F_{T_Y} + \left(Y_\beta\left(\Delta\beta + \beta_g\right) + Y_p\left(\Delta p + p_g\right) + Y_r\left(\Delta r + r_g\right) + Y_{\delta_r}\Delta\delta_r + Y_{\delta_f}\Delta\delta_f\right) = m\cdot\left(u_s\Delta\dot{\beta} + \left(\Delta r + r_g\right)u_s\right) \quad (66)$$

$$-mg\sin\theta_s\Delta\theta + \Delta F_{T_Z} + \left(Z_u\left(\Delta u + u_g\right) + Z_\alpha\left(\Delta\alpha + \alpha_g\right) + Z_{\dot{\alpha}}\left(\Delta\dot{\alpha} + q_g\right) + Z_q\left(\Delta q + q_g\right) + Z_{\delta_e}\Delta\delta_e + Z_{\delta_f}\Delta\delta_f\right) = m\left(u_s\left(\Delta\dot{\alpha} + q_g\right) - \left(\Delta q + q_g\right)u_s\right) \quad (67)$$

$$\Delta L_T + \left(L_\beta\left(\Delta\beta + \beta_g\right) + L_p\left(\Delta p + p_g\right) + L_r\left(\Delta r + r_g\right) + L_{\delta_r}\Delta\delta_r + L_{\delta_f}\Delta\delta_f\right) = I_x\Delta\dot{p} - I_{xz}\Delta\dot{r} \quad (68)$$

$$\Delta M_T + \left(M_u\left(\Delta u + u_g\right) + M_\alpha\left(\Delta\alpha + \alpha_g\right) + M_{\dot{\alpha}}\left(\Delta\dot{\alpha} + q_g\right) + M_q\left(\Delta q + q_g\right) + M_{\delta_e}\Delta\delta_e + M_{\delta_f}\Delta\delta_f\right) = I_y\Delta\dot{q} \quad (69)$$

$$\Delta N_T + \left(N_\beta\left(\Delta\beta + \beta_g\right) + N_p\left(\Delta p + p_g\right) + N_r\left(\Delta r + r_g\right) + N_{\delta_r}\Delta\delta_r + N_{\delta_f}\Delta\delta_f\right) = I_z\Delta\dot{r} - I_{xz}\Delta\dot{p} \quad (70)$$

Where $\alpha_g = w_g/u_s$ and $\beta_g = v_g/u_s$, and, once again, (65-70) can be expressed in the typical state-space matrices A and B analogously to (22-27).

D. EIGENVALUES TOWARDS THE AUTOPILOT DESIGN

Once the dynamic models have been explained, it is time to address the autopilot architecture design. The first step is to establish the design criteria in accordance to the regulation.

In Table 8 the positive imaginary part of the eigenvalues of the ATLANTE RPA are shown. As it can be seen, the short period and roll modes are in accordance with level 1 regulation requirements. Although the spiral mode is also in accordance with level 1, it is possible to stabilise it with

TABLE 8. ATLANTE RPA eigenvalues.

Mode	Pole	Damping	Frequency (rad/s)	Time Constant (s)
Phugoid	-0.03+0.26i	0.11	0.27	33.5
Short Period	-1.54+2.99i	0.46	3.36	0.65
Spiral	0.01	-1.00	-	-92.3
Roll	-7.04	1.00	-	0.14
Dutch roll	-0.12+2.29i	0.05	2.29	8.26

the autopilot. However, the Dutch roll mode does not fit the regulation requirements, and it is necessary to make improvements.

E. CERTIFIABLE AUTOPILOT DESIGN

From the certification standpoint, there are many different requisites that must be demonstrated, making essential the FTC strategy selection. For example, many research efforts in FTC use strategies that change online the gains of the controllers adapting them to the aircraft new dynamic model with specific algorithms which do not provide predefined gains values. In addition, the dynamic model after the failure happening is sometimes estimated. The estimation is made using other algorithms whose results cannot be predicted and they could be not as accurate as they should be. Therefore, the controllers based on the previous assumptions cannot pass the certification process because they do not demonstrate the certification requirements in every considered scenario. The MMST technique has been selected in this work due to its capability to switch between predefined autopilots. In addition, this technique has a rapid response for changing the autopilot configuration, which in the aviation field is critical. Each predefined autopilot is valid and certifiable for each failure scenario, inside the boundaries where the models are accurate enough. So, a high accuracy of the dynamic models of each considered scenario is also necessary to pass the certification process. These three aspects: MMST technique, classical autopilots, and accurate models provide the autopilot developed in this work the certification compliance capability.

With all the requirements in mind, the autopilot design is addressed. One original contribution of this manuscript is the certification approach to the FTC problem. The inner loop of the control architecture is the Stability Augmentation System (SAS) as it is presented in Fig. 8. In Fig. 9, the response of the aircraft to the step input in pitch rate is shown. As it can be seen, the phugoid transient response has been removed with the SAS.

The next closed-loop is the attitude controller. In this case, the pitch angle is controlled for the longitudinal problem, and the Aileron-Rudder Interconnect (ARI) system has been used for the lateral-directional one. This system is depicted in Fig. 10.

The bank angle response of the flaperon failure scenario to the step input is shown in Fig. 11. As it is demonstrated, the system is in accordance with level 1 of the regulation

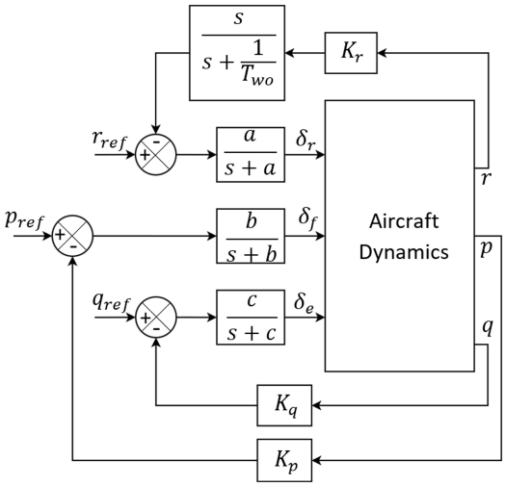

FIGURE 8. SAS architecture.

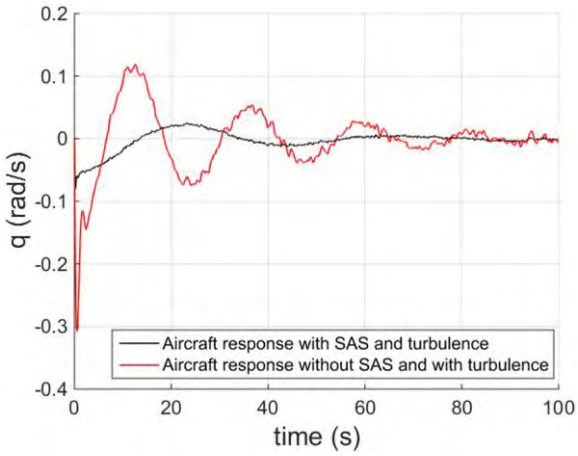

FIGURE 9. Response of the aircraft with and without the SAS to the step input in pitch rate (q_{ref}) (with turbulence).

requirements. Also, in Fig. 12, the Angle of Sideslip (AoS) is presented for the same input, showing the coordinated turns capability of the aircraft after the attitude control system design.

Finally, the path controller loop is designed. This controller is responsible for tracking the altitude and bearing. The diagram of the complete autopilot system is shown in Fig. 13. The response to the bearing reference angle of the flaperon failure scenario is included in Fig. 14.

In the case of the flaperon lock-in-place fault, the autopilot architecture is the same as in the fault-free case, but changing the PIDs gains to those that allow the autopilot to meet the certification requirements. However, it is necessary to establish another path tracking controller for the total power loss. In this case, the altitude controller has been substituted by a speed-on-elevator controller, as it is shown in Fig. 15. The response of this system with a proportional term was not sufficient to achieve the required accuracy, so an integral term has been added. The speed-on-elevator controller proposed in

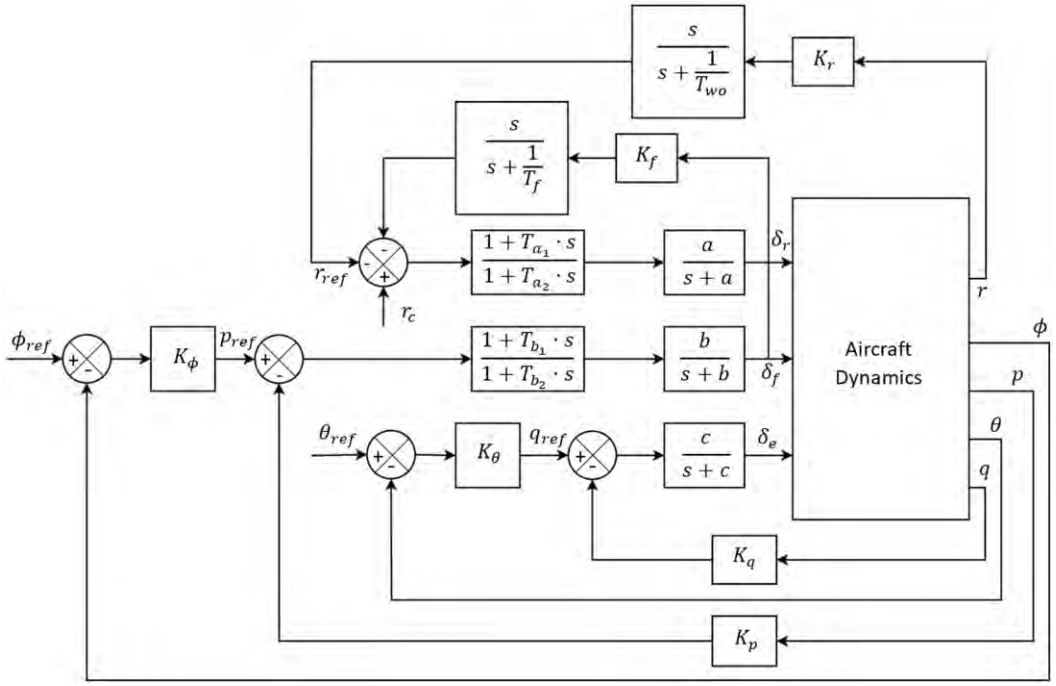

FIGURE 10. Attitude controller diagram.

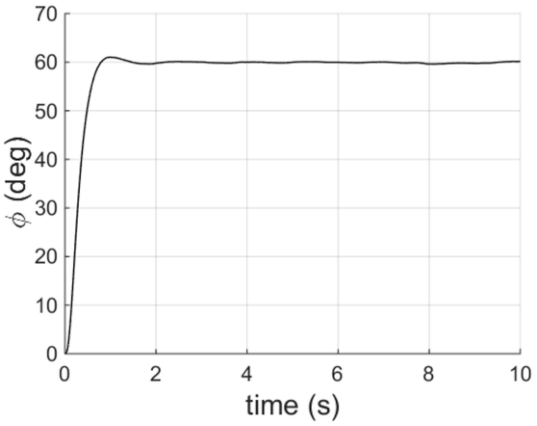

FIGURE 11. Response of the aircraft with the SAS and the ARI system to the step input in bank angle (ϕ_{ref}) (with turbulence).

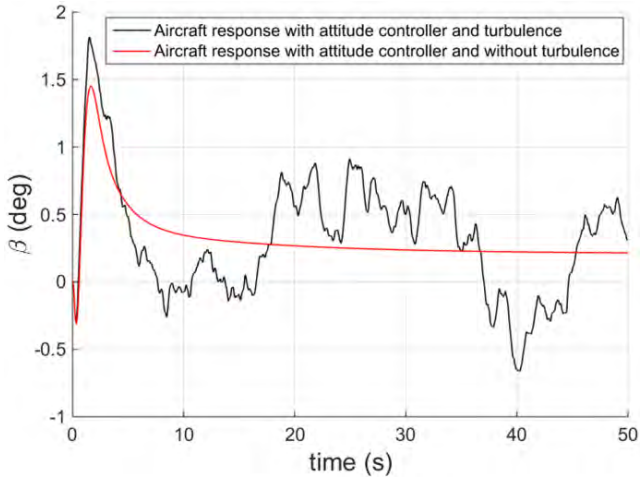

FIGURE 12. Response of the AoS (β) of the aircraft with the SAS and the ARI system to the step input in bank angle (ϕ_{ref}).

this manuscript is another original contribution. The response of this system to the step input of 10 m/s is shown in Fig. 16. This system commands a lower pitch angle in the case that the reference speed is higher than the aircraft speed, increasing the descent rate.

To conclude the autopilot design, in Table 9, which is included in the Appendix, the PIDs gains that change in each failure case are included. As the rudder and the elevator roles can be interchanged, the parameters ''a'' and ''c'' of the actuator dynamics must be the same, and their value is the most critical one. Table 10 presents the positive imaginary part of the poles of the whole closed-loop system for the flaperon fault scenario. This table is also located in the appendix. The poles that could represent the Dutch roll mode (rows three to six) satisfy the Dutch roll regulation requirements of Table 4. Analogously, the short period is one of the poles of rows four to six, and once more all these poles satisfy the short period regulation, which was presented in Table 1. As it has been demonstrated in Fig. 12, the spiral mode is stable, which is also confirmed by the negative value of the real part of all poles. The roll performance requirement has been demonstrated with Fig. 11, while the roll-mode could be one of the poles that satisfy the time constant requirement values of Table 3. Therefore, the values of this table highlight the

TABLE 9. Gains change depending on the failure scenario.

Gain	Fault-free	Flaperon failure	Powerplant failure
K_p	1	-2.5	1
K_ϕ	7	-10	7
K_f	-1.25	-0.75	-1.25
T_{b1}	0.6	0.4	0.6
T_{b2}	1	2	1
K_ψ	1.7	2.1	1.7

TABLE 10. Poles of the whole close-loop system.

Pole	Damping	Frequency (rad/s)	Time Constant (s)
-9.11e-2+2.61e-9i	1.00	0.09	11.00
-9.11e-2+9.21e-9i	1.00	0.09	11.00
-5.51e-1+8.37e-1i	0.55	1.00	1.81
-3.59+2.5i	0.82	4.37	0.28
-13.6+9.93i	0.81	16.8	0.07
-10.2+11.5i	0.67	15.4	0.10
-1.00	1.00	-	1.00
-8.89	1.00	-	0.11
-10.5	1.00	-	0.10
-2.57	1.00	-	0.39
-1.20	1.00	-	0.83
-1.90	1.00	-	0.53
-0.05	1.00	-	21.9
-0.33	1.00	-	3.05
-0.07	1.00	-	13.7
-4.77	1.00	-	0.21
-0.09	1.00	-	11.00
-0.09	1.00	-	11.00
-6.36	1.00	-	0.16
-0.09	1.00	-	11.00
-0.09	1.00	-	11.00
-0.09	1.00	-	11.00
-4.77	1.00	-	0.21

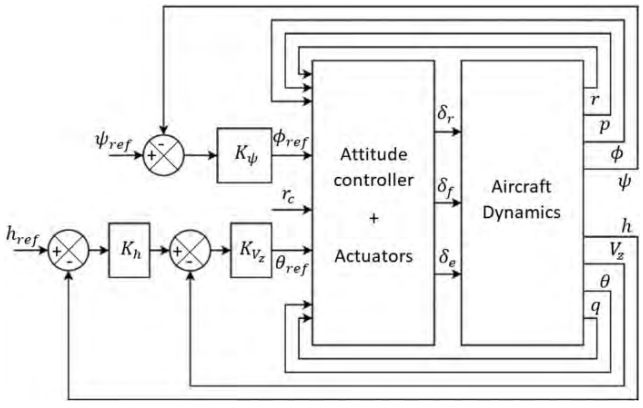

FIGURE 13. Path controller system.

concordance between the results and the regulation requirements in terms of the aircraft eigenvalues damping, frequency and time constant.

The complete blocks diagram of the Guidance, Navigation, and Control (GNC) system used in this work, including the developed MMST FTC, is shown in Fig. 17.

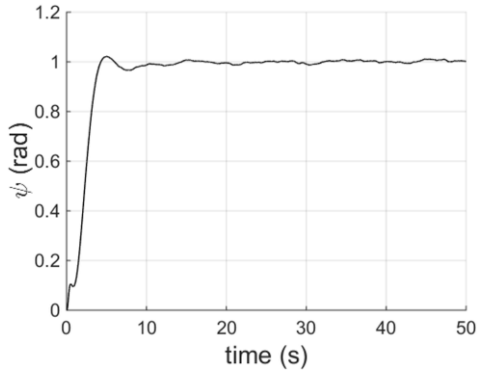

FIGURE 14. Response of the aircraft with the SAS, the ARI system and the path controller to the step input in yaw angle (ψ_{ref}) (with turbulence).

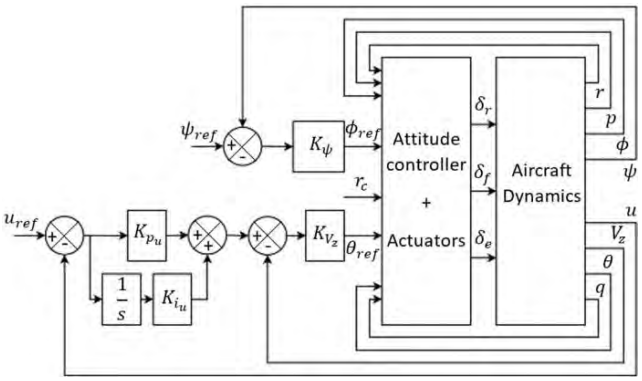

FIGURE 15. Speed-on-elevator controller diagram.

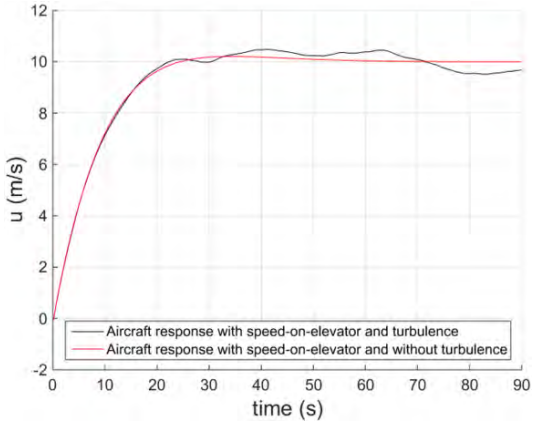

FIGURE 16. Response of the aircraft with the SAS, the ARI system and the speed-on-elevator controller to the step input in longitudinal speed (u_{ref}).

F. GUIDANCE SYSTEM RECONFIGURATION STUDY

At this moment, all the systems contained in Fig. 17 have been addressed, except the reconfigurable guidance system. The FDI and sensors and filters systems have been considered as ideal. The aircraft dynamics has been explained in Section III in detail, whereas the MMST FTC and actuators design has been addressed in the previous section. Finally, the actuators management system is responsible for commanding the

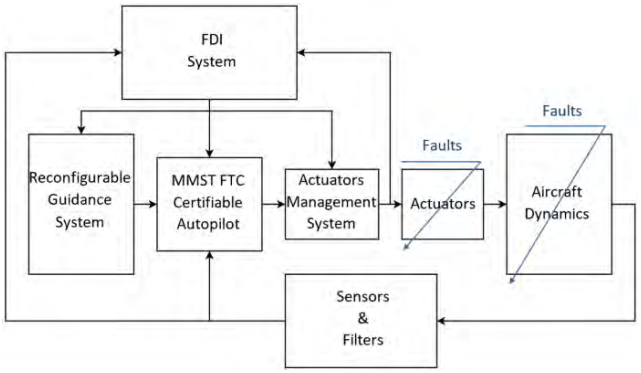

FIGURE 17. Complete diagram of the fault-tolerant GNC system.

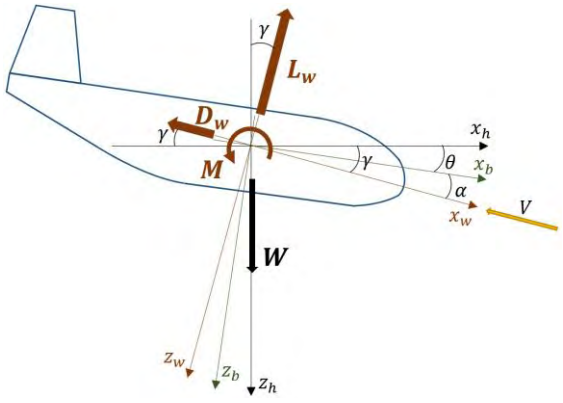

FIGURE 18. Gliding performance variables.

trim position plus the autopilot deflections of the control surfaces.

Next, a study about the reconfiguration of the guidance system has been conducted. This study and the implemented guidance reconfiguration are original contributions of this work. In the case of locked-in-place flaperon, the aircraft can finish the mission or be safely recovered without problems. Nevertheless, after total power loss, the aircraft can only follow a gliding trajectory. The main longitudinal forces and moments for the gliding trajectory are explained in Fig. 18. The expressions to describe the gliding performances without acceleration are:

$$\frac{W}{0.5\rho V^2 S_{ref}} = C_{L_{cruise}} = C_{L_W}\cos\gamma + C_{D_W}\sin\gamma \tag{71}$$

$$0 = C_{D_W}\cos\gamma - C_{L_W}\sin\gamma \tag{72}$$

$$0 = C_{m_0} + C_{m_\alpha}\alpha + C_{m_{\delta_e}}\delta_e + C_{m_{\delta_{r_{trim}}}}\delta_{r_{trim}} + C_{m_{\delta_f}}\delta_f \tag{73}$$

$$C_{D_W} = A + BC_{L_{cruise}} + DC_{L_{cruise}}^2 + C_{D_{\delta_f}}\delta_f + C_{D_{\delta_e}}\delta_e + C_{D_{\delta_{r_{trim}}}}\delta_{r_{trim}} \tag{74}$$

$$C_{L_W} = C_{L_0} + C_{L_\alpha}\alpha + C_{L_{\delta_e}}\delta_e + C_{L_{\delta_{r_{trim}}}}\delta_{r_{trim}} + C_{L_{\delta_f}}\delta_f \tag{75}$$

Where "A", "B", and "D" terms are the drag polar coefficients estimated by Torenbeek method, and $W = mg$ is

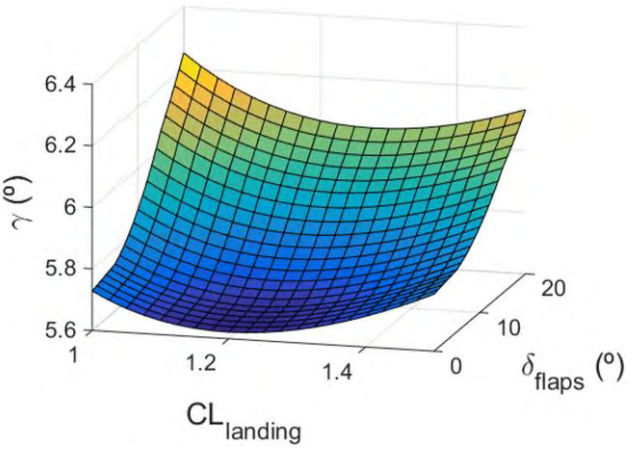

FIGURE 19. Gliding descent angle during final approach in relation to the lift coefficient and the flaps deflection.

the weight of the aircraft. The critical phase of this flight condition is the landing, which also is the worst phase for the accidents and incidents happening, as was explained in the introduction. In order to safely recover the aircraft, once the loss of power has happened, it is very important to extend the flight as much as possible to maximise the possibility of finding a safe recovery zone. Making use of (72), it is possible to express the descent angle as:

$$\tan\gamma = C_{D_W}/C_{L_W} = 1/E_{aerodynamic} \tag{76}$$

As it can be seen, the descent angle is proportional to the inverse of the aerodynamic efficiency. That is, it is possible to minimise the descent angle by maximizing the aerodynamic efficiency. Therefore, the new guidance system must estimate the required speed to achieve a lift coefficient that maximises the aerodynamic efficiency. Using the information of Fig. 3, that lift coefficient is $C_L = 1.2$. However, it is usual that the maximum aerodynamic efficiency is near-stall conditions. Because of that, the lift coefficient would be lower to increase the safety of the operation. Also, protections against stall speed have been considered. These protections compare the speed provided by the guidance system with the safe speed, which consists of the stall speed increased by a certain percentage. If the speed estimated by the guidance system is lower than the defined safe speed, then the safe speed is commanded. In any other case, the speed of the guidance system is commanded.

It is important to conduct a detailed study for the final approach and the landing phase, too. The previous guidance is valid for the gliding phase, but not when the aircraft is close to the ground. As the simulations have demonstrated, the aircraft pitch angle during the descent is negative, which could lead to a catastrophic touchdown. Additionally, it is desirable to reduce the speed before the landing phase. To do this, the flaperons can be deflected as flaps, but leaving sufficient range of movement as ailerons to alleviate the possible gusts and turbulence. Once the flaperons have been deflected

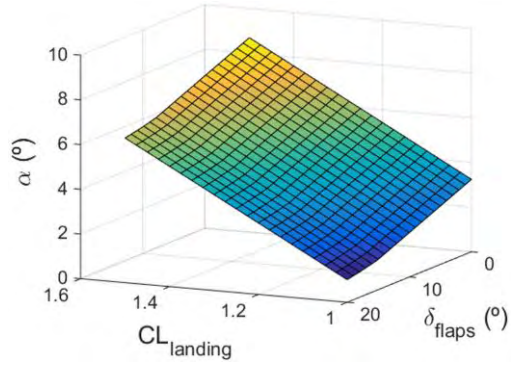

FIGURE 20. AoA during final approach in relation to the lift coefficient and the flaps deflection.

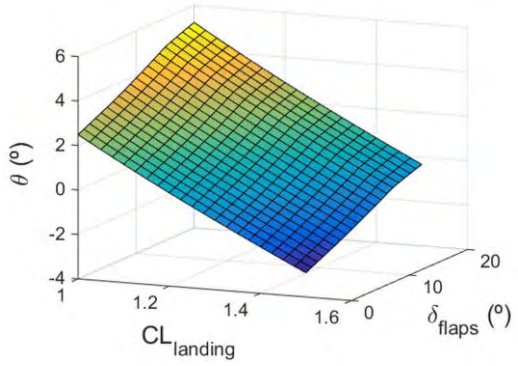

FIGURE 21. Pitch angle during final approach in relation to the lift coefficient and the flaps deflection.

as flaps and the speed has been reduced, the last change is to command a positive pitch angle to ensure that the main landing gear is the first part of the aircraft to touch the ground. Thus, it is necessary to reconfigure the autopilot once again, deactivating the speed-on-elevator controller, and activating the pitch angle controller. In other terms, deactivating the path control system and activating the attitude controller. It is important to note that the flaps deflection produces a negative pitching moment that must be compensated by the elevator to maintain the required speed. As a result of this, the elevator may not have enough range of movement to provide sufficient positive pitching moment to command the required pitch angle for the touchdown. The way to solve this situation, once more, is using the rudder deflection as an elevator. If the cross-wind during final approach is not too severe, it is possible to trim the rudder as an elevator at an intermediate position, always guaranteeing a certain range of movement for the rudder to carry out coordinated turns required by the autopilot or the possible remaining cross-wind. The results of this study are presented in the next figures. Fig. 19 shows the descent angle in relation with the lift coefficient and the flaps deflection, according to the Fig. 18. The Angle of Attack (AoA) is presented in Fig. 20. The pitch angle is included in Fig. 21. Finally, the elevator deflection without deflecting the rudder as an elevator and deflecting it to a

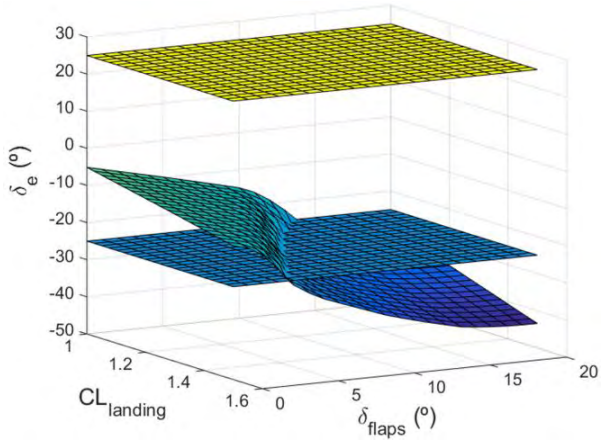

FIGURE 22. Elevator deflection without rudder trim as elevator during final approach in relation to the lift coefficient and the flaps deflection.

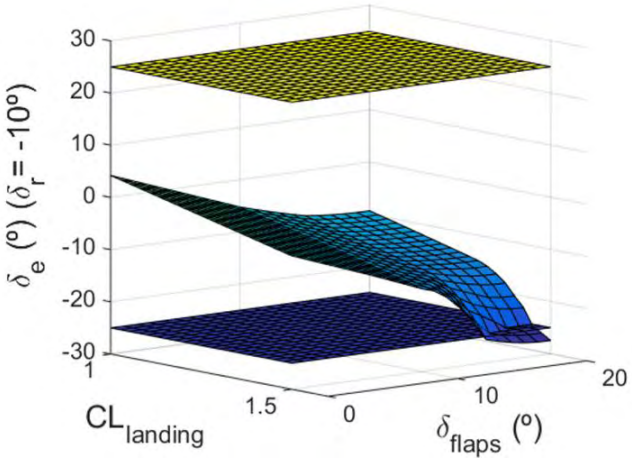

FIGURE 23. Elevator deflection with rudder trim as elevator during final approach in relation to the lift coefficient and the flaps deflection.

−10° position is depicted in Fig. 22 and Fig. 23, respectively. The rapid decrease of the control surface values is due to its effectiveness. As it is shown, the deflection of the rudder as an elevator allows the elevator to maintain itself in the linear region, making it possible to trim the aircraft.

The horizontal planes of Fig. 22 and Fig. 23 represent the safe limits for deflecting the ruddervator. The altitude for the deflection of the flaps has been established at 250 m, and the change from the speed-on-elevator control to the pitch controller is implemented at 100 m of altitude. For the landing run, each landing gear leg has been modeled through its compression transfer function for the normal force estimation. The reaction of the ground on each wheel is taken into account by combining the brakes and the friction force, which depends on the normal force and the friction coefficient. This model is based on [43].

IV. FLIGHT SIMULATOR RESULTS

In this section, different simulations are shown to check the validity of the FTC and guidance reconfiguration results.

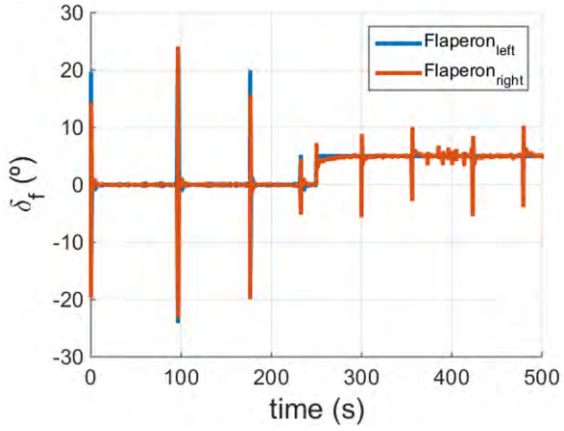

FIGURE 24. Flaperons position of the flaperon lock-in-place fault simulation.

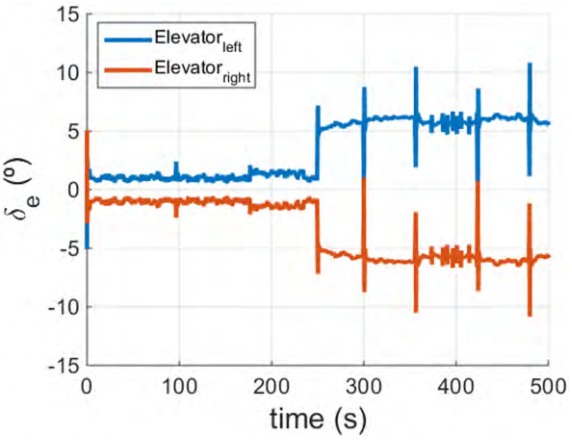

FIGURE 25. Elevator position of the flaperon lock-in-place fault simulation.

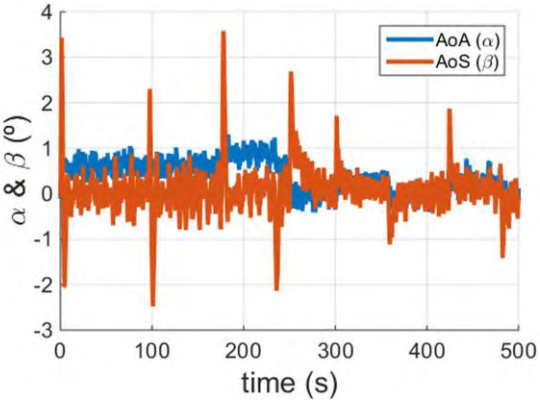

FIGURE 26. AoA and AoS of the flaperon lock-in-place fault simulation.

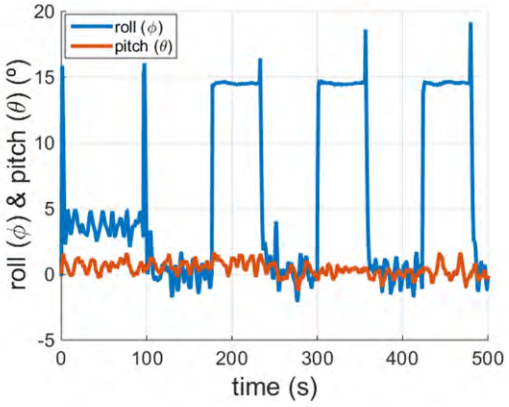

FIGURE 27. Roll and pitch angles of the flaperon lock-in-place fault simulation.

All the figures of this section are included in the appendix. The first simulation shows the flaperon fault during the loiter phase around an aerodrome. Thus, the guidance system is based on the racetrack flight procedures established by the International Civil Aviation Organization (ICAO) in [48], making use of the expressions developed by Vincenty [49] about the navigation over an ellipsoid, and the VHF Omnidirectional Range (VOR) and Distance Measuring Equipment (DME) navigation aid systems. The FDI system is assumed to be ideal, and the failure is instantly detected and identified. The actuators management system is in charge of implementing the control surfaces positions that are requested by the MMST FTC autopilot and its trim subsystem. Additionally, turbulence model is included in this simulation. The values for the turbulence model have been selected according to the worst possible scenario, which is the ''severe'' case and it makes reference to storm conditions. The flight conditions for the test are the same as for the autopilot design: constant aircraft speed of 48 m/s (TAS) and the altitude is also constant whose value is 3000 m. Finally, taking into account all the previous assumptions and considerations, the trajectory of the aircraft and its attitude are shown in the figures of the appendix in order to validate the results. In addition, the AoA and the AoS, and the control surfaces position are included.

As it can be seen in Fig. 24, the flaperon failure has happened at $t = 250$ s of the simulation. Once the left flaperon is locked-in-place, the trim subsystem requests a deflection of the remaining actuators according to the trim considerations explained in Section II of this paper. That is, the right flaperon is trimmed at 5° as flap, and then is behaving as an aileron from this position. Also, it is necessary to trim the elevator to a position of $-5.4°$. The AoA changes its value in this new condition, as expressions (1-3) predicted. The elevator deflection is included in Fig. 25. The AoA and AoS are presented in Fig. 26. For the attitude behaviour of the aircraft, the roll and pitch angles are shown in Fig. 27. To conclude with the first simulation results, the latitude and longitude positions during the simulation are shown in Fig. 28.

The powerplant failure explained in Section II is validated in the second simulation. In this case, the FDI system is also ideal, and the actuators management system behaviour is analogous to the first simulation, but considering the particularities of the powerplant failure condition. The guidance system is reconfigured after the failure as was explained in

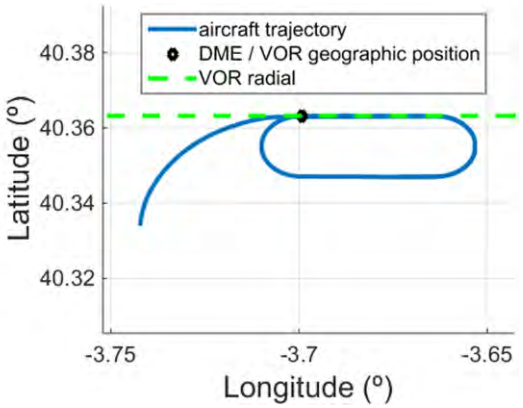

FIGURE 28. Latitude and longitude of the flaperon lock-in-place fault simulation.

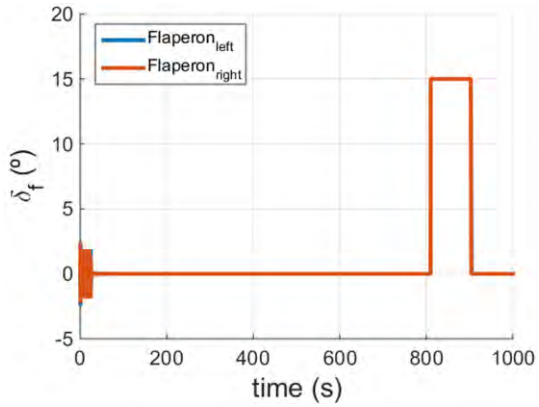

FIGURE 29. Flaperons position of the powerplant failure simulation.

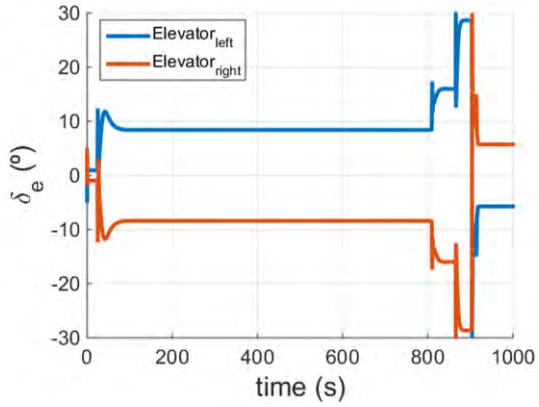

FIGURE 30. Elevator position of the powerplant failure simulation.

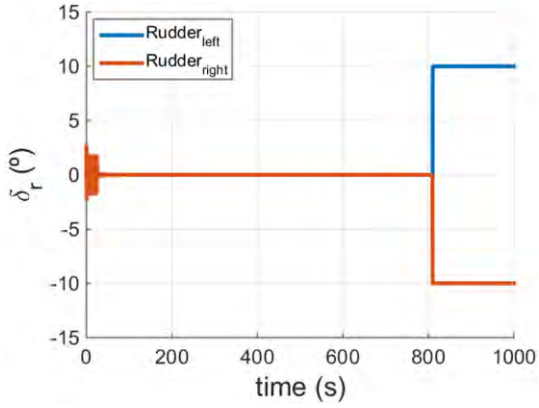

FIGURE 31. Rudder position of the powerplant failure simulation.

Section IV. For this simulation, the turbulence model has been deactivated, which allows for comparison of the response of the aircraft with turbulence of the first simulation and the response of the aircraft without turbulence of this second simulation. In addition, the results can be checked more precisely because there is no turbulence noise in the response. At $t = 30$ s the powerplant is broken down, and then the propeller is feathered by adjusting its pitch angle at 82°, which provides a final drag coefficient increment of $\Delta C_D = 0.0019$, according to the drag model due to a stopped propeller [44]. In the case that the propeller could not be feathered, the drag increment for a blades pitch angle of 45° is $\Delta C_D = 0.0097$, giving an increase of 14.6% of the "A" drag polar coefficient. As it can be seen, the drag increase due to a stopped propeller must not be neglected. If the feathering of the propeller is not possible, both the aerodynamic efficiency ($E_{aerodynamic}$) and the travelled longitudinal distance until the final landing would be smaller. The initial flight condition for this simulation is the same condition as in the previous case. However, after the powerplant failure, the aircraft loses altitude and flies at the speed commanded by the reconfigured guidance system until the final approach and the landing. At an altitude of 250 m the flaperons are deflected as flaps at a position of 15°, leaving 10° for the behaviour as ailerons. When the altitude is lower than 100 m, the autopilot is reconfigured to control the pitch angle, and then a reference positive pitch is commanded to ensure that the main landing gear is the first in touching the ground. During the landing run, the brakes of the wheels are activated to reduce the speed of the aircraft more effectively.

Flaperons, elevator, and rudder positions are included in Fig. 29, in Fig. 30, and in Fig. 31, respectively. As shown, the elevator is deflected almost to its maximum position for commanding a final positive pitch angle of 2°. The reason the elevator does not have enough command power to provide a greater pitch angle is the pitching moment provided by the flaperons as flaps, whose value is -0.191. In Fig. 32, the AoA and the AoS are presented. The final step of the AoA is due to the ground reaction on the landing gear. When the main landing gear touches the ground, the aircraft experiences a vertical speed, resulting in a decreasing in the AoA and the climb angle. The roll, pitch and yaw angles are shown in Fig. 33. For the trajectory of the aircraft, the altitude evolution is included in Fig. 34. Finally, the speed is contained in Fig. 35. As it can be seen, there are two steps at the end of the gliding flight in the speed. The first step is due to the flaperon deflection as flaps, and the pitch controlling is the reason for the second step. The final quick decreasing in the speed corresponds to the landing run. The final longitudinal travelled distance has

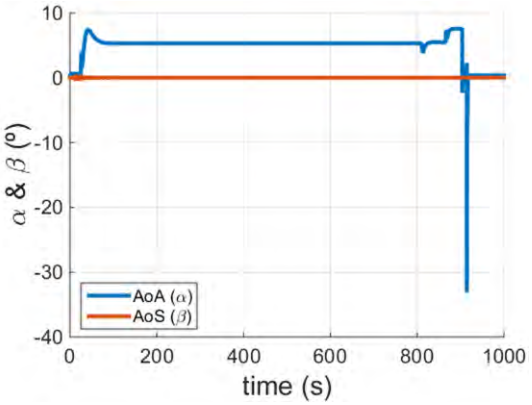

FIGURE 32. AoA and AoS position of the powerplant failure simulation.

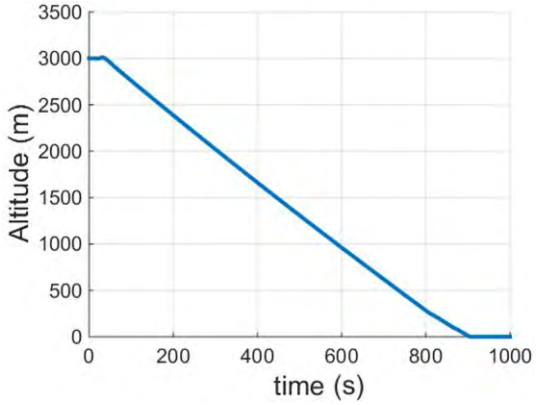

FIGURE 34. Altitude of the powerplant failure simulation.

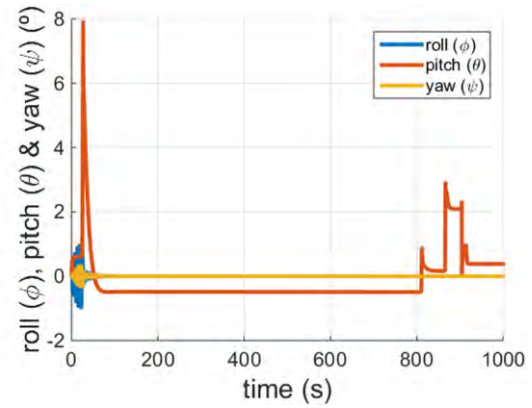

FIGURE 33. Roll, pitch, and yaw angles of the powerplant failure simulation.

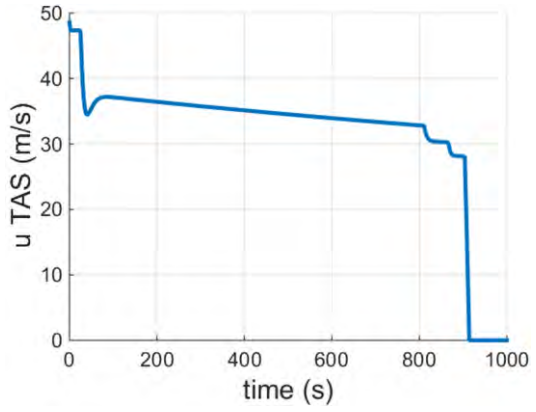

FIGURE 35. Longitudinal speed of the powerplant failure simulation.

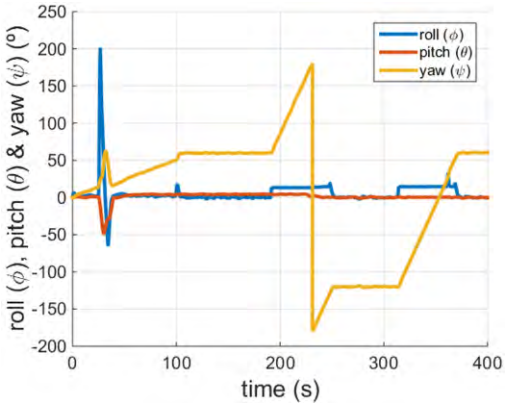

FIGURE 36. Roll, pitch and yaw angles of the flaperon lock-in-place fault simulation with 0.875 s detection and identification time of the FDI system.

been 30450 m since the powerplant failure happening (gliding flight), whereas the landing run distance has been 145 m.

Finally, a study about the maximum allowable reconfiguration time of the FTC has been conducted from an aircraft control standpoint. In the previous simulations, the FDI system was taken as an ideal system which instantly identified the presence of failure. Nevertheless, the time that the FDI system expends in the detection and identification of failure presence could become critical depending on the kind of failure. In the next study, a delay has been implemented between the failure happening and its identification by the FDI system. Making use of this delay, it is possible to consider that the FDI is not ideal any more, and thus, it expends certain amount of time in the failure detection and identification. This study is an original contribution of this paper.

For the flaperon failure studied in this work, as the reconfiguration of the autopilot needs the change of the sign of some PIDs gains, the time for the reconfiguration must be small. The maximum time allowed to identify the failure is around 0.875 s. However, for the powerplant failure, where the only change is the altitude controller, the time to identify this kind of failure only becomes critical when the aeroplane flies at low altitudes, in ground proximity conditions. That is because the altitude lost by the aircraft could result in the flight toward terrain. Fig. 36 presents the roll, pitch and yaw angles for the flaperon failure at $t = 25$ s in the case of a delay of 0.875 s in the identification, whereas Fig. 37 contains the AoA and AoS. For the same conditions, the latitude and longitude positions, the altitude, and the aircraft speed are presented in Fig. 38, in Fig. 39, and in Fig. 40, respectively.

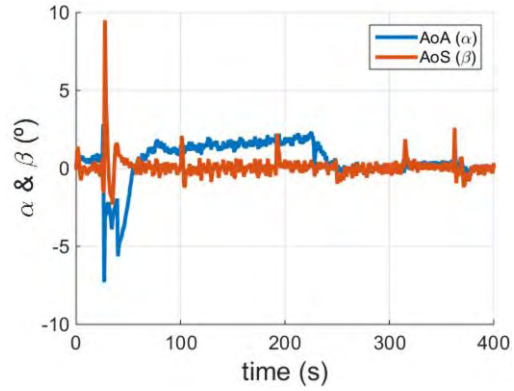

FIGURE 37. AoA and AoS of the flaperon lock-in-place fault simulation with 0.875 s detection and identification time of the FDI system.

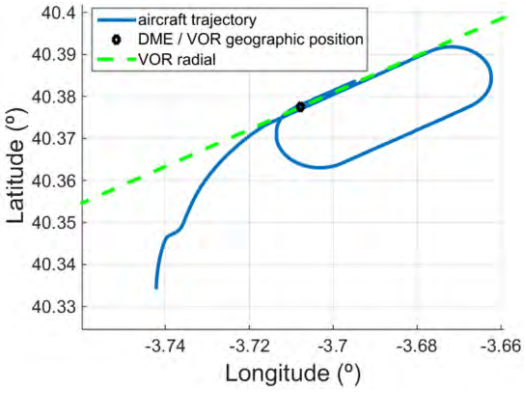

FIGURE 38. Latitude and longitude of the flaperon lock-in-place fault simulation with 0.875 s detection and identification time of the FDI system.

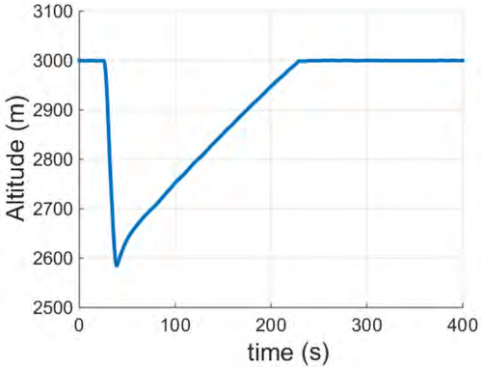

FIGURE 39. Altitude of the flaperon lock-in-place fault simulation with 0.875 s detection and identification time of the FDI system.

As these figures show, the altitude loss and the speed increase are not negligible, while the trajectory of the aircraft is almost the same.

A mitigation alternative could be the deactivation of the autopilot for the aerodynamic control surfaces when a failure is detected until its identification. Once the identification is achieved, the reconfiguration is possible and implemented. Additionally, it is necessary to establish limits to the vertical

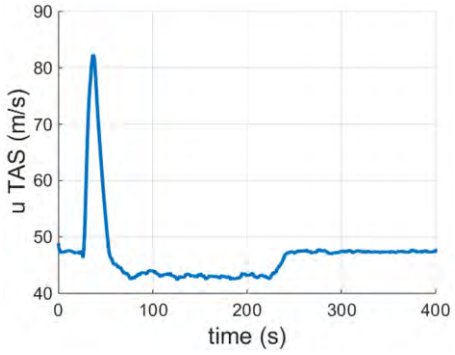

FIGURE 40. Longitudinal speed of the flaperon lock-in-place fault simulation with 0.875 s detection and identification time of the FDI system.

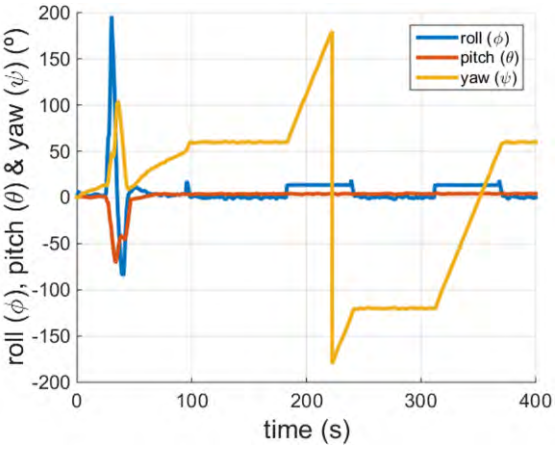

FIGURE 41. Roll, pitch and yaw angles of the flaperon lock-in-place fault simulation with 5 s identification time of the FDI system and deactivating the autopilot after the failure detection.

speed (rate of climb, V_z in this case) and the roll rate (p) to obtain a good response from the aircraft control point of view. If this saturation is not implemented, then the autopilot commands excessive deflections of the controls after the failure identification and the aircraft could be uncontrollable. Further investigations about the maximum allowable manoeuvres should be conducted in order to ensure that ultimate loads are not achieved in the transient response after the failure happening and until its identification, and so, ensuring that there is no structural damage presence. As in the previous case, the results for the simulation with flaperon failure at $t = 25$ s are presented in the figures of the appendix. The detection of the failure is instantaneous, but the identification is achieved 5 s after the failure happening. Roll, pitch and yaw angles are presented in Fig. 41, the AoA and the AoS are shown in Fig. 42, the latitude and longitude positions are included in Fig. 43, the altitude is shown in Fig. 44, and the speed of the aircraft is contained in Fig. 45. As these figures show, the proposed mitigation alternative results in an increase of the allowed identification time, which improves the safe operation of the aeroplane.

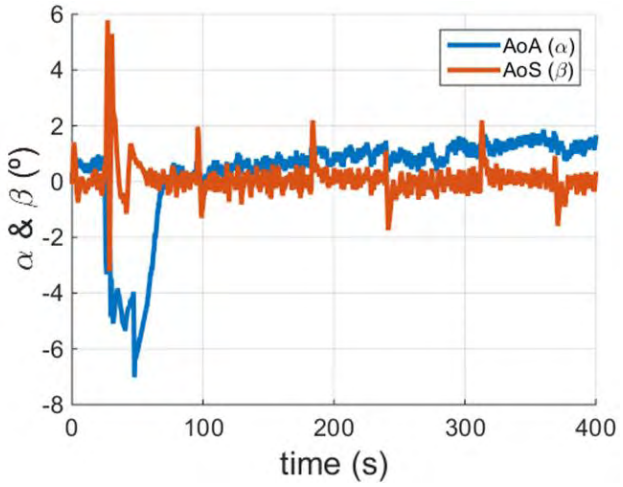

FIGURE 42. AoA and AoS of the flaperon lock-in-place fault simulation with 5 s identification time of the FDI system and deactivating the autopilot after the failure detection.

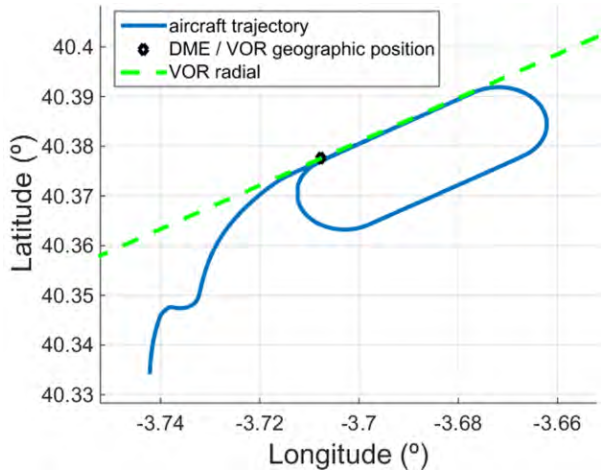

FIGURE 43. Latitude and longitude of the flaperon lock-in-place fault simulation with 5 s identification time of the FDI system and deactivating the autopilot after the failure detection.

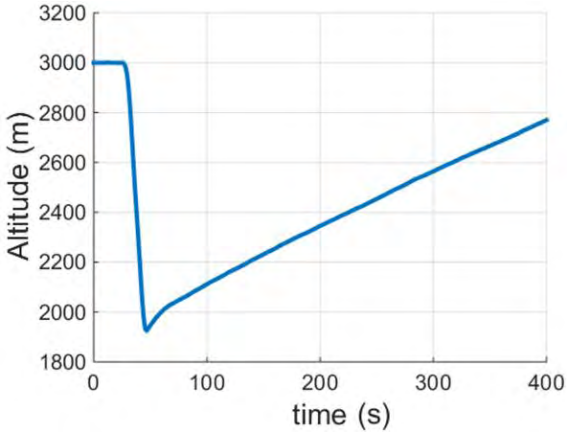

FIGURE 44. Altitude of the flaperon lock-in-place fault simulation with 5 s identification time of the FDI system and deactivating the autopilot after the failure detection.

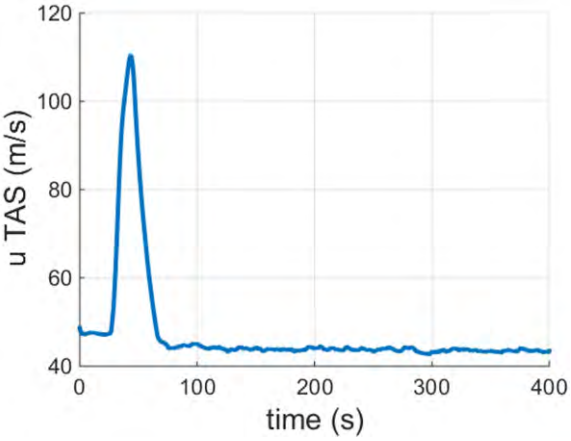

FIGURE 45. Longitudinal speed of the flaperon lock-in-place fault simulation with 5 s identification time of the FDI system and deactivating the autopilot after the failure detection.

Finally, a study about the detection and identification time of the state-of-the-art has been conducted to check the viability of the previous results. According to [50], the detection time is a percentage of time over the window of 2 s the authors use to detect failures, even in the presence of moderate turbulence. The time for detection and identification is improved in [7], where the expended time by the FDI system in the detection and identification is 0.5 s. Finally, the time for the same both processes of detection and identification is 0.025 s in [13] and [51]. In addition, faults are rapidly and reliably detected and identified taking into account severe and low turbulence in [52]. As it can be seen, the detection and identification time requirements identified with the simulations of this work are satisfied by the state-of-the-art FDI systems capabilities.

To conclude with this section, the simulations conducted in this paper are compared to similar simulations of the state-of-the-art presented in the introduction. It is important to note that the aircraft dynamics differs for aircraft of different categories. So, if aircraft of different categories are compared, the results could vary significantly. On the one hand, in this work the left flaperon is locked-in-place at a 5° position, whereas the aileron effectiveness becomes reversed in [1], and aileron lock-in-place and hardover failures are considered in [11]. The aircraft can follow the desired path of the final approach phase in [1] even in the presence of gust effects. The trajectory is a coordinated turn at an altitude of 5000 ft and a speed of 70 m/s during 30 s. The controller gains are determined from the response of the nominal aircraft without failures by the authors. As they say, it is difficult to prove the stability and convergence criteria of the total system using the parameter estimation combined with nonlinear controller. So, the controller gains are selected to allow sufficient stability margin to the nominal system. The trajectory tracking performance is deteriorated with a lock-in-place fault of more than 20° or hardover for the inner

aileron of a Boeing 747 with the baseline CA, but not with the redistributed CA, in [11]. The redistributed CA technique is based on the use of CA technique in combination with fuzzy logic to correlate between the faults and the control redistribution. The simulations conducted were only for the lateral-directional problem with a linear-based controller. In fact, the only variables shown are the bank angle and the angle of sideslip. Additionally, for an outer aileron lock-in-place fault, the stability is only guaranteed when redistributed CA and ramp input on the bank angle are used, depending on the rate of change for each lock-in-place failure. The authors established the nonlinear environment, the FDI system delay or the engine thrust integration into the control loop as future works of their research. The failures considered in these references can be addressed with satisfactory results using the procedure followed in this work, in the same way as it has been demonstrated for the flaperon lock-in-place failure. Furthermore, the turbulence effects have been taken into account in this manuscript, whereas the two previous references have not included them. In the case of flap failures, this kind of failure is addressed without much detail in [6], where the authors only say the basic MPC is relatively robust to the flap fault. Trailing edge flaps failure is also considered in [8] in two different scenarios: one false alarm failure and another lock-in-place failure; and leading edge flaps failure which is not detected by the FDI system is addressed, too. However, there are only some results of the lateral-directional variables for each kind of fault which include 30 s once the failure or the false alarm has happened. The lateral-directional states did not show adverse effects in any failure scenario. On the other hand, the total power loss is the powerplant failure addressed in this work, whereas engine separation scenario is considered in [9]. As it can be seen, the failure scenarios are different, so the guidance system reconfiguration is also different, although in both cases the aircraft can follow the trajectory demanded by the guidance system after the failure happening. The authors used online nonlinear dynamic model identification in combination with adaptive nonlinear ID to control the aircraft. The aircraft of the engine separation scenario is a Boeing 747 that lost two of its four engines, therefore it still had enough thrust to command the required flight path. However, as it has been shown along this paper, the powerplant failure of this work results in a gliding flight, making essential the reconfiguration of both the autopilot and the guidance system. In addition, the trajectory followed in this work includes the final approach and the landing phase, which are not considered in [9].

V. CONCLUSION

Throughout this paper the complete procedure to address the Fault-Tolerant Control (FTC) design for RPAS has been presented. Different innovations have been included in this manuscript as the certifiable fault-tolerant autopilot design or the reconfiguration of the guidance system.

As it was said in the introduction and in Section III-E, there are issues with the certification requirements demonstration of the FTC systems. Nevertheless, this goal has been accomplished with the Multiple Model Switching and Tuning (MMST) technique in combination with classical autopilots, and the use of accurate models of the aircraft in the presence of the considered failures.

The possibility of certifying the fault-tolerant autopilots in the same way as classical certification process has been confirmed. This new FTC approach could be a very important step in the integration of RPAS in non-segregated airspace, especially those with greater Maximum Take-Off Weight (MTOW). The relevance of each kind of failure for the certifiable autopilot development depends on the design mission of the aircraft, at is was explained in Section II. Furthermore, the strategy followed in this research, in particular the proposed powerplant failure solution, could be applied to general manned aviation in order to reduce the number of human casualties in many accidents.

Additionally, the dynamic models explained in this paper after the failure presence could be used in many other kinds of failure scenarios by modifying the corresponding terms of the models. Asymmetric failures require the addition of the cross-terms between the longitudinal and lateral-directional problems. In this paper, these problems are coupled after the flaperon failure through the control matrix B terms, as it was explained in Section III. However, an asymmetric structural element loss results in a coupling in the state-space matrix A, which is not addressed in this work.

Finally, the study related to the allowed time for failure identification by the Fault Detection and Identification (FDI) system shows the viability of the autopilot reconfiguration.

APPENDIX

See Tables 9 and 10.
See Figs. 24–45.

REFERENCES

[1] N. Tanaka, S. Suzuki, K. Masui, and H. Tomita, "Restructurable guidance and control for aircraft with failures considering gust effects," *J. Guid. Control. Dyn.*, vol. 29, no. 3, pp. 671–679, 2006.
[2] C. Hajiyev and F. Caliskan, "Sensor and control surface/actuator failure detection and isolation applied to F-16 flight dynamic," *Aircraft Eng. Aerosp. Technol.*, vol. 77, no. 2, pp. 152–160, 2005.
[3] C. Hajiyev and H. E. Soken, "Robust adaptive kalman filter for estimation of UAV dynamics in the presence of sensor/actuator faults," *Aerosp. Sci. Technol.*, vol. 28, no. 1, pp. 376–383, 2013.
[4] R. Hallouzi and M. Verhaegen, "Fault-tolerant subspace predictive control applied to a boeing 747 model," *J. Guid. Control. Dyn.*, vol. 31, no. 4, pp. 873–883, 2008.
[5] C. Rago, R. Prasanth, R. K. Mehra, and R. Fortenbaugh, "Failure detection and identification and fault tolerant control using the IMM-KF with applications to the eagle-eye UAV," in *Proc. 37th IEEE Conf. Decision Control*, vol. 4. Tampa, FL, USA, Dec. 1998, pp. 4208–4213.
[6] M. Gopinathan, J. D. Boskovic, R. K. Mehra, and C. Rago, "A multiple model predictive scheme for fault-tolerant flight control design," in *Proc. 37th IEEE Conf. Decision Control*, vol. 2. Tampa, FL, USA, Dec. 1998, pp. 1376–1381.
[7] J. D. Boskovic, S. Li, and R. K. Mehra, "Robust supervisory fault-tolerant flight control system," in *Proc. Amer. Control Conf.*, Arlington, TX, USA, Jun. 2001, pp. 1815–1820.
[8] J. D. Boskovic, J. Redding, and R. K. Mehra, "Stable adaptive reconfigurable flight control with self-diagnostics," in *Proc. Amer. Control Conf.*, New York, NY, USA, Jul. 2007, pp. 5765–5770.

[9] T. J. J. Lombaerts, H. O. Huisman, Q. P. Chu, J. A. Mulder, and D. A. Joosten, "Nonlinear reconfiguring flight control based on online physical model identification," *J. Guid. Control. Dyn.*, vol. 32, no. 3, pp. 727–748, 2009.

[10] M. E. N. Sørensen, S. Hansen, M. Breivik, and M. Blanke, "Performance comparison of controllers with fault-dependent control allocation for UAVs," *J. Intell. Robot. Syst.*, vol. 87, no. 1, pp. 187–207, 2017.

[11] S. H. Almutairi and N. Aouf, "Reconfigurable dynamic control allocation for aircraft with actuator failures," *Aeronaut. J.*, vol. 121, no. 1237, pp. 341–371, 2017.

[12] J. D. Boskovic, S.-M. Li, and R. K. Mehra, "Reconfigurable flight control design using multiple switching controllers and online estimation of damage-related," in *Proc. IEEE Int. Conf. Control Appl.*, Anchorage, AK, USA, Sep. 2000, pp. 479–484.

[13] J. D. Boskovic and R. K. Mehra, "A multiple model-based reconfigurable flight control system design," in *Proc. 37th IEEE Conf. Decision Control*, vol. 4. Tampa, FL, USA, Dec. 1998, pp. 4503–4508.

[14] Y. Wang, L. Yang, J. Zhang, and G. Shen, "A multivariable adaptive reconfigurable control method applied to the wing damaged aircraft," in *Proc. IEEE Int. Conf. Control Autom. (ICCA)*, Hangzhou, China, Jun. 2013, pp. 95–100.

[15] X. Li and H. H. T. Liu, "A passive fault tolerant flight control for maximum allowable vertical tail damaged aircraft," *J. Dyn. Syst. Meas. Control*, vol. 134, no. 3, p. 31006, 2012.

[16] J. Wang, S. Wang, X. Wang, C. Shi, and M. M. Tomovic, "Active fault tolerant control for vertical tail damaged aircraft with dissimilar redundant actuation system," *Chin. J. Aeronaut.*, vol. 29, no. 5, pp. 1313–1325, 2016.

[17] C. Edwards, T. Lombaerts, and H. Smaili, *Fault Tolerant Flight Control a Benchmark Challenge*, 1st ed. Luxembourg: Springer, 2010.

[18] *Operation and Certification of Small Unmanned Aircraft Systems*, document FAR Part 107, Fed. Aviation Admin. (FAA), Washington, DC, USA, 2016.

[19] *Introduction of a Regulatory Framework for the Operation of Drones*, document NPA 2017-05, Eur. Aviation Safety Agency (EASA), Cologne, Germany, 2017.

[20] *Introduction of a Regulatory Framework for the Operation of Drones*, document A-NPA 2015-10, Eur. Aviation Safety Agency (EASA), Cologne, Germany, 2015.

[21] *Aerospace—Flight Control Systems—Design, Installation and Test of Piloted Military Aircraft, General Specification for*, SAE Standard AS94900, SAE Int., Warrendale, PA, USA, 2007.

[22] *Flight Control Systems—Design, Installation and Test of Piloted Aircraft, General Specification for*, document MIL-DTL-9490E, USAF, Warrendale, PA, USA, 2008.

[23] *Flying Qualities of Piloted Airplanes*, document MIL-F-8785C, USAF, Wright-Patterson AFB, OH, USA, 1980.

[24] *Statistical Summary of Commercial Jet Airplane Accidents*, Boeing Commercial Airplanes, Seattle, WA, USA, 2015.

[25] *Annual Review 2015*, Comisión Invest. Accidentes Incidentes Aviación Civil (CIAIAC), Madrid, Spain, 2016.

[26] *Accidents During Flight Instruction: A Review*, Air Safety Inst., Frederick, MD, USA, 2014.

[27] *Annual Safety Review 2016*, Eur. Aviation Safety Agency (EASA), Cologne, Germany, 2016.

[28] *Annual Safety Review 2017*, Eur. Aviation Safety Agency (EASA), Cologne, Germany, 2017.

[29] J. F. Portilla, "Investigación de accidentes de aeronaves no tripuladas—RPAS," M.S. thesis, Dept. Aircraft Spacecraft, ETSI Aeronáutica y del Espacio, UPM, Madrid, Spain, 2014.

[30] K. W. Williams, "A summary of unmanned aircraft accident/incident data: Human factors implications," Fed. Aviation Admin. (FAA), Oklahoma, OK, USA, Tech. Rep. DOT/FAA/AM-04/24, 2004.

[31] M. Asim, D. N. Ehsan, and K. Rafique, "Probable causal factors in UAV accidents based on human factor analysis and classification," in *Proc. 27th Int. Congr. Aeronaut. Sci. (ICAS)*, Nice, France, 2010, pp. 1–6.

[32] *ATLANTE: Tactical Unmanned Aerial System for National Security*, Cassidian, Unterschleißheim, Germany, 2014, pp. 1–2.

[33] *ATLANTE: Tactical Fixed Wing Multirole UAS for Maximized Operational Capability and Mission Flexibility*, Airbus Defence & Space, Toulouse, France, 2014, pp. 1–2.

[34] E. Torenbeek, *Synthesis of Subsonic Airplane Design*, 1st ed. Delft, The Netherlands: Delft Univ. Press, 1976.

[35] L. M. Nicolai and G. E. Carichner, *Fundamentals os Aircraft and Airship Design: Aircraft Design*, vol. 1, 1st ed. Blacksburg, VA, USA: AIAA, 2010.

[36] McDonell Douglas Corporation (Douglas Aircraft Division), *The USAF Stability and Control Digital DATCOM*, vols. 1–3, 1st ed. Wright-Patterson Air Force Base, OH, USA: USAF, 1979.

[37] J. Roskam, *Methods for Estimating Stability and Control Derivatives of Conventional Subsonic Airplanes*, 2nd ed. Lawrence, AR, USA: Roskam Aviation Engineering Corporation, 1973.

[38] J. Roskam, *Airplane Design: Part 6*, 1st ed. Lawrence, AR, USA: Roskam Aviation Engineering Corporation, 1987.

[39] D. P. Raymer, *Aircraft Design: A Conceptual Approach*, 3rd ed. Sylmar, CA, USA: AIAA, 1999.

[40] P. E. Purser and J. P. Campbell, "Experimental verification of a simplified vee-tail theory and analysis of available data on complete models with vee-tails," NACA, Langley Field, VA, USA, NACA Rep. 823, 1944.

[41] National Advisory Committee for Aeronautics (NACA), "Propeller-efficiency charts for light airplanes," NACA, Langley Field, VA, USA, NACA Rep. 1338, 1947.

[42] L. García-Hernández *et al.*, "Developing models for future real-time platforms: Virtual simulation and design of new components and systems for aircraft and remotely piloted aircraft systems," in *Proc. IEEE Int. Conf. Ind. Technol.*, Seville, Spain, Mar. 2015, pp. 1996–2003.

[43] M. Baarspul, "A review of flight simulation techniques," *Prog. Aerosp. Sci.*, vol. 27, no. 1, pp. 1–120, Jan. 1990.

[44] S. Gudmundsson, *General Aviation Aircraft Design: Applied Methods and Procedures*, 1st ed. Waltham, MA, USA: Elsevier, 2014.

[45] J. Roskam, *Airplane Flight Dynamics and Automatic Flight Controls: Part I*, 3rd ed. Lawrence, AR, USA: DARcorporation, 2001.

[46] R. E. McFarland, *Finite Element Aircraft Simulation of Turbulence*. Moffett Field, CA, USA: NASA, 1997.

[47] *Flying Qualities of Piloted Aircraft*, document MIL-HDBK-1797, U.S. Dept. Defense, Washington, DC, USA, 1997.

[48] *Aircraft Operations: Flight Procedures*, document 8168, Int. Civil Aviation Org. (ICAO), Montréal, BC, Canada, 2006, vol. 1.

[49] T. Vincenty, "Direct and inverse solutions of geodesics on the ellipsoid with application of nested equations," *Surv. Rev.*, vol. 23, no. 176, pp. 88–93, 1975.

[50] D. Wong, S. Poll, and K. KrishnaKumar, "Aircraft fault detection and classification using multi-level immune learning detection," in *Proc. Infotech Aeros.*, Reston, VA, USA, 2005, pp. 1–14.

[51] Z. Zhengdao and Z. Weihua, "Neural network based fault detection and identification for fighter control surface failure," in *Proc. Chin. Control Decis. Conf.*, Guilin, China, Jun. 2009, pp. 5256–5261.

[52] D. G. Dimogianopoulos, J. D. Hios, and S. D. Fassois, "Aircraft fault detection and identification by stochastic functionally pooled modelling of relationships among attitude data," *Proc. Inst. Mech. Eng., G, J. Aerosp. Eng.*, vol. 222, no. 6, pp. 801–816, 2008.

LUIS GARCÍA-HERNÁNDEZ was born in Madrid, Spain, in 1989. He received the M.S. degree in aerospace engineering from the Universidad Politécnica de Madrid, Madrid, in 2014, where he is currently pursuing the Ph.D. degree in aerospace engineering.

Since 2013, he has been collaborated in different research studies at the Aircraft and Spacecraft Department, Universidad Politécnica de Madrid. He has authored several papers in relation to RPAS, conceptual and preliminary aircraft design, flight physics or flight simulators, among others. His research interests include fault-tolerant control and reconfigurable guidance systems applied to RPAS, flight simulators, conceptual, preliminary, and hardware-in-the-loop tools development, aviation regulations referred to both manned and unmanned aircraft, and innovation RPAS applications.

CRISTINA CUERNO-REJADO was born in Madrid, Spain, in 1963. She received the M.S.Eng. degree in aeronautical engineering in 1987 and the Ph.D. degree (Hons.) in aeronautical engineering from the Universidad Politécnica de Madrid, Madrid, in 1992.

From 1997 to 1995, she was a Lecturer, and from 1995 to 2016 she was an Associate Professor with the Universidad Politécnica de Madrid, where she has been a Full Professor since 2016. In parallel, she has also been the Deputy Director for External Relations at the Faculty of Aerospace Engineering. She has participated in more than 50 research projects and contracts, has authored over 40 international papers, and has participated in over 50 international congresses and conferences. She is an expert in the field of aircraft design, where she has developed extensive research in the fields of conceptual design of unconventional aeroplanes, structural design of unconventional aeroplanes, and conceptual design of remotely piloted aerial systems. In particular, she is a specialist in the areas of airworthiness and multidisciplinary optimization applied to aircraft design. Since 2010, she has been a member of the Board of the Spanish Air Accidents and Incidents Investigation Commission.

MANUEL PÉREZ-CORTÉS received the M.S. and Ph.D. degrees in aeronautical engineering from the Universidad Politécnica de Madrid in 1982 and 1985, respectively, and the M.B.A. degree from the Business School IESE.

He has been with the company Grupo Mecánica del Vuelo (GMV), Madrid, Spain, since 1985. He was involved in several fields, especially developing applications for the aerospace, and defense and security sectors, both in satellite navigation systems and training as well as research and engineering simulators of various types of vehicles, or command and control systems and, generally, in the integration of information systems. He has held different positions at GMV and he is currently the General Manager of Homeland Security and Defense. Since 1987, he has been an Associate Professor with the ETSI Aeronáutica y del Espacio, Universidad Politécnica de Madrid. He is currently the Director of the Spanish School of Tests in Flight and Airworthiness. His research interests include applications development for aerospace, and defense and security sectors, different kinds of vehicle simulators, and command and control systems.